Response to review comments on acp-2016-453 from reviewer 2

The original comments are provided in black, our response is given below each comment in red.

Thank you for the careful reading of our manuscript and your review.

Summary

The present work investigates how an increase in spatial (horizontal) resolution from 60 km to 12 km improves the ability of a mesoscale simulation with the WRF-Chem model to reproduce satellite observations of aerosol optical depth (AOD) and column concentrations of chemical species, and of key meteorological variables (relative to a reanalysis product). The WRF-Chem model is run for the year 2008 on a domain that covers the eastern USA, a region with strong emissions of natural and anthropogenic aerosol precursors.

The motivation of the work is established in the introduction. Simulations, observations, and reanalysis data are subsequently introduced with select relevant details, such as uncertainties in the satellite observations. The authors then provide an overview of the statistical methods used to evaluate model performance relative to observations and reanalysis in a succinct but effective way, which can serve as an introduction to novices to the subject. In the main part of the work the results are presented and analyzed, and the authors carefully quantify and discuss the improvements from an increase in resolution. It is found that a higher simulation resolution improves model fidelity in reproducing observed AOD as well as the ability of the model to identify extreme AOD values. The analysis reveals that the improved performance of the model at higher resolution can in part be attributed to improved agreement in meteorological quantities, in particular boundary layer specific humidity, which contributes to aerosol growth. The model is also shown to better reproduce satellite observations of chemical species at higher resolution. The authors do not fail to identify instances where a higher resolution does not result in an improvement: While model skill (measured by the Brier skill score) in reproducing AOD improves in seven out of twelve months, the model shows improvements in detecting extreme AOD values only in the warm season. In all this, statistical methods are used effectively to quantify model performance. The work addresses an interesting question of general importance in atmospheric modeling - what improvements can be expected from an increase in model resolution? The authors answer this question in exemplary fashion for aerosol properties, chemistry, and meteorology in a mesoscale model. The key insight is that increased spatial (horizontal) resolution clearly improves model performance but is not a panacea. Model aspects other than resolution need attention as well to improve model fidelity. The manuscript is thorough, clear, compelling, very well written, and presents the results with good figures and tables. I recommend publication after attending to the following detailed comments.

Thank you for your positive assessment. We have addressed your detailed comments below and modified the manuscript accordingly.

Detailed comments

Line 51-52: Please give references for the possible range of values for the direct and indirect aerosol effects.

Thanks for noting this. We have now added the following reference:

Stocker, T. F. a. Q., D. and Plattner, G.-K. and Alexander, L.V. and Allen, S.K. and Bindoff, N.L. and Bréon, F.-M. and Church, J.A. and Cubasch, U. and Emori, S. and Forster, P. and Friedlingstein, P. and Gillett, N. and Gregory, J.M. and Hartmann, D.L. and Jansen, E. and Kirtman, B. and Knutti, R. and Krishna Kumar, K. and Lemke, P. and Marotzke, J. and Masson-Delmotte, V. and Meehl, G.A. and Mokhov, I.I. and Piao,

S. and Ramaswamy, V. and Randall, D. and Rhein, M. and Rojas, M. and Sabine, C. and Shindell, D. and Talley, L.D. and Vaughan, D.G. and Xie, S.-P. (2013), Summary for Policymakers, in *Climate Change 2013: The Physical Science Basis. Contribution of Working Group I to the Fifth Assessment Report of the Intergovernmental Panel on Climate Change*, edited, pp. 33–115, Cambridge University Press, Cambridge, United Kingdom and New York, NY, USA.

Section 2.1: Aerosol size distributions are generally log-normal, not power law functions. The upper tail of a log-normal distribution does, however, behave like a power law distribution. The discussion here is therefore not incorrect, however, it should be modified to assume a log-normal distribution (also because the aerosol scheme used in the WRF-Chem simulations assumes log-normal distributions).
Thanks for this comment. We rephrased the paragraph as follows:

The relationship between the aerosol size distribution and spectral dependence of AOD is described by a power law function:

$$\beta(\lambda) = \beta(\lambda_0) \times \lambda^{-\alpha} \quad \textbf{(1)}$$

where β is the particle extinction coefficient, λ is the wavelength (λ_0=1μm) and α is the Ångström exponent (Ångström, 1964) which describes the wavelength dependence of AOD (and is inversely proportional to the average aerosol diameter Dp):

$$\alpha = \frac{\ln \frac{AOD(\lambda_1)}{AOD(\lambda_2)}}{\frac{\lambda_2}{\lambda_1}} \quad \textbf{(2)}$$

The aerosol volume distribution (and thus also its size distribution) can be often described as a multi-lognormal function with *n* modes:

$$\frac{dV(r)}{d\ln r} = \sum_{i=1}^{n} \frac{C_i}{\sqrt{2\pi}\sigma_i} \exp\left[\frac{-(\ln r - \ln R_i)^2}{2\sigma_i^{\,2}}\right] \quad \textbf{(3)}$$

where C_i is the particle volume concentration in the mode *i*, R_i is the geometric mean radius and σ_i is the geometric standard deviation, thus we have:

$$AOD(\lambda) = \int \frac{3\beta(m,r,\lambda)}{4r} \frac{dV(r)}{d\ln r} d\ln r dZ \quad \textbf{(4)}$$

As indicated in (Schuster, 2006), "the spectral variability of extinction diminishes for particles larger than the incident wavelength", thus fine mode particles contribute more to AOD in the visible (λ~0.5 μm) than at longer wavelengths, whereas coarse mode particles provide a similar AOD both at short and long wavelengths. This is reflected in the Ångström parameter which can be thus used as a proxy for the fine mode fraction or fine mode radius (Schuster, 2006).

Line 417-418: "Further, the seasonal average spatial patterns of the total columnar concentrations, expressed in terms of z-scores, also exhibit high qualitative agreement with the satellite observations (Fig. S4-S7)."
It is a stretch to write "high qualitative agreement" here. Comparing the OMI, WRF60, and WRF12-remap panels in Fig. S4-S7, my impression is that omitting "high" and leaving "qualitative agreement" is a more accurate assessment.
We agree. We modified the text accordingly and removed "high".

Table 1: A factor of 9 is placed in the denominator of the Bonferroni correction, but the data at the different wavelengths, resolutions, and remappings would not seem to be truly independent significance tests. For example, WRF12 and WRF12-remap would seem to be very dependent. Please carefully consider (and justify) whether the factor of 9 should be used or rather omitted.

We agree that some of the simulations are not really independent as also are the twelve months of the year. The Bonferroni correction can be applied to any set of experiments, either dependent or independent, and aims at providing the most conservative indication of the significance of a statistical test. Therefore we decided to keep the original significance assessment (i.e. with the factor 9) and clarified the explanation of the Bonferroni correction by removing the reference to independence at line 225 as follows:

"To assess the significance of ρ while accounting for multiple testing, we apply a Bonferroni correction (Simes, 1986) in which for *m* hypothesis tests, the null hypothesis is rejected if $p \leq \frac{\alpha}{m}$, where *p* is the p-value and α is the confidence level (0.05 is used here)."

Figure S5: OMI, WRF60, and WRF12-remap panels (or panel titles) are shuffled relative to the panel order in Figures S4, S6, and S7.
Thanks for pointing this. We have now reordered the panels to be consistent with the other figures on the gas phase evaluation.

Value-added by high-resolution regional simulations of climate-relevant aerosol properties

P. Crippa[1], R. C. Sullivan[2], A. Thota[3], S. C. Pryor[2,3]

[1]COMET, School of Civil Engineering and Geosciences, Cassie Building, Newcastle University, Newcastle upon Tyne, NE1 7RU, UK
[2]Department of Earth and Atmospheric Sciences, Bradfield Hall, 306 Tower Road, Cornell University, Ithaca, NY 14853, USA
[3]Pervasive Technology Institute, Indiana University, Bloomington, IN 47405, USA

Correspondence to: P. Crippa (paola.crippa@ncl.ac.uk), School of Civil Engineering and Geosciences, Cassie Building, Room G15, Telephone: +44 (0)191 208 5041, Newcastle University, Newcastle upon Tyne, NE1 7RU, UK

Abstract

Despite recent advances in global Earth System Models (ESMs), the current global mean aerosol direct and indirect radiative effects remain uncertain, as does their future role in climate forcing and regional manifestations. Reasons for this uncertainty include the high spatio-temporal variability of aerosol populations. Thus, limited area (regional) models applied at higher resolution over specific regions of interest are generally expected to 'add value', i.e. improve the fidelity of the physical-dynamical-chemical processes that induce extreme events and dictate climate forcing, via more realistic representation of spatio-temporal variability. However, added value is not inevitable, and there remains a need to optimize use of numerical resources, and to quantify the impact on simulation fidelity that derives from increased resolution. Here we quantify the value added by enhanced spatial resolution in simulations of the drivers of aerosol direct radiative forcing by applying the Weather Research and Forecasting model with coupled Chemistry (WRF-Chem) over eastern North America at different resolutions. Using Brier Skill Scores and other statistical metrics it is shown that enhanced resolution (from 60 to 12 km) improves model performance for all of the meteorological parameters and gas phase concentrations considered, in addition to both mean and extreme Aerosol Optical Depth (AOD) in three wavelengths in the visible relative to satellite observations, principally via increase of potential skill. Some of the enhanced model performance for AOD appears to be attributable to improved simulation of specific humidity and the resulting impact on aerosol hygroscopic growth/hysteresis.

Keywords: added value, high-resolution WRF-Chem simulations, aerosol optical properties, extreme AOD

1 Motivation and Objectives

Aerosols alter Earth's radiation balance primarily by scattering or absorbing incoming solar radiation (direct effect, dominated by accumulation mode (diameters ~ wavelength (λ), where total extinction is often quantified using AOD), or regulating cloud formation/properties by acting as cloud condensation nuclei (CCN) (indirect effect, dominated by diameters ≥ 100 nm, magnitude = f(composition)). Most aerosols (excluding black carbon) have a larger scattering cross-section than absorption cross-section, and act as CCN thus enhancing cloud albedo and lifetimes. Hence increased aerosol concentrations are generally (but not uniformly) associated with surface cooling (offsetting a fraction of greenhouse gas warming) (Boucher, 2013;Myhre et al., 2013b) to a degree that is principally dictated by the aerosol concentration, size and composition, in addition to the underlying surface and height of the aerosol layer (McComiskey et al., 2008). Despite major advances in measurement and modeling, both the current global mean aerosol direct effect (possible range: -0.77 to +0.23 W m^{-2}) and the indirect effect (possible range: -1.33 to -0.06 W m^{-2}) remain uncertain (Stocker, 2013), as does their future role in climate forcing (Rockel et al., 2008) and regional manifestations (Myhre et al., 2013a). Specific to our current study region (eastern N. America), one analysis using the NASA GISS global model found that the "regional radiative forcing from US anthropogenic aerosols elicits a strong regional climate response, cooling the central and eastern US by 0.5–1.0 °C on average during 1970–1990, with the strongest effects on maximum daytime temperatures in summer and autumn. Aerosol cooling reflects comparable contributions from direct and indirect radiative effects" (Leibensperger et al., 2012). A recent comparison of multiple global models conducted under the AEROCOM-project indicated this is also a region that exhibits very large model-to-model variability in simulated AOD (<AOD> ~ 0.5, σ(AOD) ~ 1) (Myhre et al., 2013a).

Major reasons why aerosol radiative forcing on both the global and regional scales remains uncertain include short atmospheric residence times and high spatio-temporal variability of aerosol populations, and the complexity of the processes that dictate aerosol concentrations, composition and size distributions (Seinfeld and Pandis, 2016). Although aerosol processes and properties are increasingly being treated in the global Earth System Models (ESMs) (Long et al., 2015;Tilmes et al., 2015) being applied in Coupled Model Intercomparison Project Phase 6 (CMIP-6) (Meehl et al., 2014), the scales on which such models are applied remain much coarser than those on which aerosol population properties are known to vary (Anderson et al., 2003). Therefore, limited area atmospheric models (regional –models)

applied at higher resolution over specific regions of interest are expected to 'add value' (i.e. improve the fidelity) of the physical-dynamical-chemical processes that induce extreme events and dictate climate forcing. There is empirical evidence to suggest strong resolution dependence in simulated aerosol particle properties. For example, WRF-Chem simulations with spatial resolution enhanced from 75 km to 3 km ~~provide~~exhibited higher correlations and lower bias relative to observations of aerosol optical properties over Mexico likely due to more accurate description of emissions, meteorology and of the physicochemical processes that convert trace gases to particles (Gustafson et al., 2011;Qian et al., 2010). ~~As a result~~This improvement in the simulation of aerosol optical properties implies, a reduction of the uncertainty in associated aerosol radiative forcing ~~will be also achieved~~ (Gustafson et al., 2011). Further, ~~when~~ WRF-Chem ~~is~~ run over the United Kingdom and Northern France at multiple resolutions in the range of 40-160 km, ~~it~~ underestimated~~s~~ AOD by 10-16% and overestimated~~s~~ CCN by 18-36% relative to a high resolution run at 10 km, partly as a result of scale dependence of the gas-phase chemistry and ~~different gas-phase chemistry and~~differences in the aerosol uptake of water (Weigum et al., 2016).

However, debate remains regarding how to objectively evaluate model performance, quantify the value added by enhanced resolution (Di Luca et al., 2015;Rockel et al., 2008) and on possible limits to the improvement of climate representation in light of errors in the driving "imperfect lateral boundary conditions" (Diaconescu and Laprise, 2013). Nevertheless, although "it is unrealistic to expect a vast amount of added values since models already performs rather decently" (Di Luca et al., 2015) and global ESMs are now run at much higher resolution than in the past, it is generally assumed that high resolution regional models will add value via more realistic representation of spatio-temporal variability than global coarser-resolution simulations. Further, "the main added value of a regional climate model is provided by its small scales and its skill to simulate extreme events, particularly for precipitation" (Diaconescu and Laprise, 2013). ~~(Qian et al., 2010)(Gustafson et al., 2011)~~

Here we quantify the value added by enhanced resolution in the description of the drivers of aerosol direct radiative forcing using year-long simulations from WRF-Chem over eastern North America. The primary performance evaluation focuses on AOD at ~~the~~ different wavelengths (λ = 470, 550 and 660 nm, where the AOD at different λ is used as a proxy of the aerosol size distribution (Tomasi et al., 1983), see details in Sect. 2.1) and is measured relative to observations from satellite-borne instrumentation. Thus the term "value added" is used here to refer to an improvement of model performance in simulation of wavelength

specific AOD as measured by the MODerate resolution Imaging Spectroradiometer (MODIS) instrument aboard the polar-orbiting Terra satellite. We begin by quantifying the performance of WRF-Chem when applied over eastern North America at a resolution of 60 km (WRF60) (~ finest resolution likely to be employed in CMIP-6 global simulations) and then compare the results to those from simulations conducted at 12 km (WRF12) (simulation details are given in Table 1~~Table S1~~). Quantification of model skill is undertaken by mapping the WRF12 output to the WRF60 grid (WRF12-remap) and computing Brier Skill Scores (BSS) using MODIS as the target, WRF60 as the reference forecast and WRF12-remap as the forecast to be evaluated. We also evaluate the impact of simulation resolution on extreme AOD values that are associated with enhanced impacts on climate and human health. This analysis uses both *Accuracy* and *Hit Rate* as the performance metrics and focuses on the co-occurrence of extreme values in space from the model output and MODIS.

Our final analysis focuses on evaluation of the value-added by enhanced resolution in terms of key meteorological and gas-phase drivers of aerosol concentrations and composition and is conducted relative to the MERRA-2 reanalysis product for the physical variables and columnar gas concentrations from satellite observations (see details of the precise data sets used given below). The meteorological parameters considered are air temperature at 2 m (T_{2m}), total monthly precipitation (*PPT*), planetary boundary-layer height (*PBLH*) and specific humidity in the boundary layer (Q_{PBL}). The gas phase concentrations considered are: sulfur dioxide (SO_2), ammonia (NH_3), nitrogen dioxide (NO_2) and formaldehyde (HCHO).

2 Materials and Methods

2.1 Spectral dependence of AOD

Three properties dictate the actual aerosol direct radiative forcing: AOD, single scattering albedo and asymmetry factor, all of which are a function of the wavelength (λ) of incident radiation. The first property is related to the total columnar mass loading, typically dominates the variability of direct aerosol effect (Chin et al., 2009) and is the focus of the current research. The relationship between the aerosol size distribution and spectral dependence of AOD is ~~discussed~~ described by a power law function:~~in detail in (Tomasi et al., 1983) but can be understood by considering a simplified example:~~

$$\beta(\lambda_1) = \beta(\lambda_2) \times \frac{\lambda_1}{\lambda_2}^{-\alpha} \quad \textbf{(1)}$$

where β is the particle extinction coefficient at a specific wavelength, λ ~~is the wavelength~~ and α is the Ångström exponent (Ångström, 1964) which describes the wavelength dependence of AOD (and is inversely proportional to the average aerosol diameter ~~Dp~~):

$$\alpha = \frac{\ln \frac{AOD(\lambda_1)}{AOD(\lambda_2)}}{\frac{\lambda_2}{\lambda_1}} \quad \textbf{(2)}$$

The aerosol volume distribution (and thus also its size distribution) usually conforms to a multi-lognormal function with n modes:

$$\frac{dV(r)}{d\ln r} = \sum_{i=1}^{n} \frac{C_i}{\sqrt{2\pi}\sigma_i} \exp\left[\frac{-(\ln r - \ln R_i)^2}{2\sigma_i^2}\right] \quad \textbf{(3)}$$

where C_i is the particle volume concentration in the mode i, R_i is the geometric mean radius and σ_i is the geometric standard deviation, thus we have:

$$AOD(\lambda) = \int \frac{3\beta(m,r,\lambda)}{4r} \frac{dV(r)}{d\ln r} d\ln r dZ \quad \textbf{(4)}$$

As indicated in (Schuster, 2006), "the spectral variability of extinction diminishes for particles larger than the incident wavelength", thus fine mode particles contribute more to AOD in the visible (λ~0.5 μm) than at longer wavelengths, whereas coarse mode particles provide a similar AOD both at short and long wavelengths. This is reflected in the Ångström parameter which can be thus used as a proxy for the fine mode fraction or fine mode radius (Schuster, 2006)~~{Ackermann, 1998 #26}~~.~~Using Mie theory for spherical particles with radius (r): 0.1-1 μm, if the aerosol size distribution is described by the Junge power law (Eq. 3) then α ~ ν-2 (i.e. α~1):~~

$$\frac{dN}{d\ln(r)} = K \times r^{-\nu} \quad \textbf{(3)}$$

~~where dN is the number of particles of size falling within the radius interval $d\ln(r)$, K is a constant (function of particle total number concentration) and ν is the Junge parameter (ν is~~

~~typically of the order of 2-3 for $r < 10$ μm and decreases with increasing proportion of coarse aerosols) (Tomasi et al., 1983). Thus, aerosol populations with a higher proportion of coarse mode aerosols will, on average, exhibit higher AOD in the longer wavelengths.(Schuster, 2006)~~

2.2 WRF-Chem simulations

WRF-Chem (version 3.6.1) simulations were performed for the calendar year 2008 over eastern North America, in a domain centered over southern Indiana (86°W, 39°N) at two resolutions, one close to the finest resolution designed for CMIP-6 global model runs (i.e. 60 km, WRF60) and the other one at much higher resolution (12 km, WRF12). Simulation settings are identical for the two runs except for the time-step used for the physics (Table 1)~~Table S1),~~. Physical and chemical parameterizations were chosen to match previous work using WRF-Chem at 12 km on the same region which showed good performance relative to observations and the year 2008 was selected because representative of average climate and aerosol conditions during 2000 - 2014 (Crippa et al., 2016). More specifically the simulations adopted the RADM2 chemical mechanism (Stockwell et al., 1990) and ~~include use of~~ a modal representation of the aerosol size distribution (MADE/SORGAM, (Ackermann et al., 1998;Schell et al., 2001)) with three lognormal modes and fixed geometric standard deviations (~~$\sigma_{g,Aitken}$~~=i.e. 1.7, ~~6 and $\sigma_{g,accumulation}$~~=2 and~~,~~ 2.5 for Aitken, accumulation and coarse mode, respectively ~~–~~(Ackermann et al., 1998;Grell et al., 2005)). Aerosol direct feedback was turned on and coupled to the Goddard shortwave scheme (Fast et al., 2006). A~~and~~ telescoping vertical grid with 32 model layers from the surface to 50 hPa and 10 ~~model~~ layers up ~~from the surface~~ to 800 hPa was selected. Meteorological initial and boundary conditions from the North American Mesoscale Model at 12 km resolution are applied every 6 hours, while initial and chemical boundary conditions are taken from MOZART-4 (Model for Ozone and Related chemical Tracers, version 4) with meteorology from NCEP/NCAR-reanalysis (Emmons et al., 2010). Anthropogenic emissions are specified for both WRF60 and WRF12 from the US National Emission Inventory 2005 (NEI-05) (US-EPA, 2009) which provides hourly point and area emissions at 4 km on 19 vertical levels. The simulation settings and specifically the use of a modal representation of the aerosol size distribution were selected to retain computational tractability. Accordingly, the 60 km simulations for the year 2008 completed in 6.4 hours whereas the 12 km simulations completed in 9.5 days (230 hours) on the Cray XE6/XK7 supercomputer (Big Red II) owned by Indiana University, using 256 processors distributed on 8 nodes.

Value added is quantified by degrading (averaging) hourly output from the 12 km resolution simulation to 60 km (hereafter WRF12-remap) as follows: the 12 km domain is resized excluding 2 grid cells at the border to exactly match the 60 km resolution domain. Each coarse grid cell thus includes 5×5 12 km resolution cells and its value is the mean of all valid 12 km grid cells inside it if at least half of those cells contain valid AOD (i.e. no cloud cover), otherwise the whole coarse cell is treated as missing. In all comparisons only cells with simultaneous (i.e. model and MODIS) clear sky conditions are considered. A daily value from WRF-Chem is computed as an instantaneous value for the hour nearest to the satellite overpass time. When the comparison is done on a monthly basis, a monthly mean value is computed from the daily values obtained~~and~~ under clear sky conditions, only if there are at least five valid observations in the month. ~~A daily value is computed for the satellite overpass time, while a monthly mean is computed using values during the overpass hour and under clear sky conditions if there are at least five valid observations in the month.~~

2.3 Observations

Model aerosol optical properties are evaluated relative to the MODIS Collection 6 dark-target land aerosol product from aboard the Terra satellite (~1030 overpass local solar time (LST)) (Levy et al., 2013). To provide a consistent assessment of model skill, the evaluation of AOD is conducted only on land areas since the MODIS dark-target ocean aerosol product is based on a retrieval algorithm different from the one over land (Levy et al., 2013). Trace gas concentrations are evaluated relative to measurements from the Ozone Monitoring Instrument (OMI; version 3) (Chance, 2002) and the Infrared Atmospheric Sounding Interferometer (IASI; NN version 1) (Whitburn, 2016) aboard the Aura (~1345 LST) and MetOp satellites (~0930 LST), respectively. MODIS retrieves AOD at multiple λ including 470, 550, and 660 nm, and t~~. T~~he MODIS algorithm removes cloud-contaminated pixels prior to spatial averaging over 10 × 10 km (at nadir). OMI and IASI have nadir resolutions of 13 × 24 km and 12 km (circular footprint), respectively, and have been filtered to remove retrievals with cloud fractions > 0.3 (Fioletov et al., 2011;McLinden et al., 2014;Vinken et al., 2014) and OMI pixels affected by the row anomalies. MODIS, OMI, and IASI provide near daily global coverage, although the row anomalies render portions of the OMI viewing swath unusable. Uncertainty in AOD from MODIS is spatially and temporally variable. It has been estimated as ~~±~~ (0.05 ~~+~~ ~~±~~ ~~0.~~15%) ~~×~~ for AOD over land (Levy et al., 2013), and prior research has reported 71% of MODIS Collection 5 retrievals fall within ~~±~~ 0.05 ~~±~~ ~~±~~ ~~0.~~20% for~~×~~ AOD relative to AERONET in the study domain (Hyer et al., 2011). The accuracy of OMI ("root

sum of the square of all errors, including forward model, inverse model, and instrument errors" (Brinksma, 2003)) is 1.1 DU or 50% for SO_2, 2 × 10^{14} cm^{-2}/30% for background/polluted NO_2 conditions, and 35% for HCHO. This uncertainty is typically reduced by spatial and temporal averaging, as ~~described below~~employed herein (Fioletov et al., 2011;Krotkov et al., 2008). IASI NH_3 retrievals do not use an a priori assumption of emissions, vertical distribution, or lifetime of NH_3 (i.e. no averaging kernel); therefore, NH_3 accuracy is variable, and thus only retrievals with uncertainty lower than the retrieved concentrations are used (Whitburn, 2016).

~~For the model evaluation,~~ For the model evaluation, satellite observations for each day are regridded to the WRF-Chem ~~domain~~discretization. This is done by averaging all valid retrievals within: 0.1° and 0.35° of the WRF-Chem grid-cell center for the 12×12 km and 60×60 km resolutions, respectively for MODIS; 0.125° × 0.18° (along-track/latitudinal × cross-track/longitudinal) and 0.365° × 0.42° for OMI; 0.12° and 0.36° for IASI ~~of each WRF-Chem grid cell centroid, for the 12×12 km and 60×60 km resolutions, respectively.~~ ~~MODIS AOD; OMI SO_2, NO_2, and HCHO; and IASI NH_3 for each day are regridded to the WRF-Chem domain by averaging all valid retrievals within 0.1° and 0.35°; 0.125° × 0.18° and 0.365° × 0.42°; and 0.12° and 0.36° of each WRF-Chem grid cell centroid, for the 12×12 km and 60×60 km resolutions, respectively.~~ To avoid issues from under-sampling, we require at least 10 valid MODIS granules for the 60×60 km daily average to be computed and at least 5 daily averages to compute a monthly average for each grid cell. Model evaluation of gaseous species is performed on a seasonal basis using standard scores (z-scores), which are computed~~computed~~ as the difference between ~~relative to~~the seasonal mean within a grid cell and the seasonal spatial mean ~~of each month~~, divided by the seasonal spatial standard deviation. The use of standard scores~~, which a~~ allows ~~comparing~~ comparison of the spatial patterns of satellite observations and model output in terms of standard deviation units from the mean.

The simulated meteorological properties are evaluated using Modern-Era Retrospective analysis for Research and Applications (MERRA-2) reanalysis data as the target. MERRA-2 is a homogenized and continuous in time description of atmospheric properties on a 3-dimensional global grid (horizontal resolution of 0.5°×0.625°, L72), developed by NASA and was released in Fall 2015 (Molod et al., 2015). MERRA-2 provides hourly values of T_{2m} and *PBLH*, and vertical profile of 3-dimensional variables every 3 hours on a large number of

pressure levels. Here we compute the total specific humidity (Q_{PBL}) of the lowest 8 pressure levels (i.e. in the boundary-layer approximated as the layer from 1000 to 825 hPa) in MERRA-2, assuming an average air density in the PBL of 1.1 kg m^{-3}. For the evaluation of simulated precipitation, we use accumulated monthly total values.

2.4 Quantification of model performance and added-value

Taylor diagrams summarize three aspects of model performance relative to a reference: the spatial correlation coefficient (i.e. Pearson correlation of the fields, r), the ratio of spatial standard deviations of the two spatial fields ($\sigma_{wrf}/\sigma_{sat}$) and the root mean squared difference (Taylor, 2001). Here Taylor diagrams are presented for monthly mean AOD from WRF60, WRF12 and WRF12-remap relative to MODIS at different wavelengths (Fig. 1 d-f). Because AOD is not normally distributed, Spearman's rank correlation coefficients (ρ) of the mean monthly AOD spatial fields are also computed to reduce the impact of a few outliers and the small sample size during cold months (Table 2~~Table 2~~~~Table 1~~). To assess the significance of ρ while accounting for multiple testing, we apply a Bonferroni correction (Simes, 1986) in which for m ~~independent~~ hypothesis tests, the null hypothesis is rejected if $p \leq \frac{\alpha}{m}$, where p is the p-value and α is the confidence level (0.05 is used here).

We further quantify the value added (or lack of thereof) of the high-resolution simulations using the following metrics:

(i) Brier Skill Score

The primary metric used to quantify the added value of WRF12-remap versus WRF60 is the Brier Skill Score (BSS) (Murphy and Epstein, 1989):

$$BSS = \frac{r_{F'P'}^2 - \left(r_{F'P'} - \frac{\sigma_{F'}}{\sigma_{P'}}\right)^2 - \left(\frac{\langle P' \rangle - \langle F' \rangle}{\sigma_{P'}}\right)^2 + \left(\frac{\langle P' \rangle}{\sigma_{P'}}\right)^2}{1 + \left(\frac{\langle P' \rangle}{\sigma_{P'}}\right)^2} \quad \textbf{(5)}$$

where F is the "forecast" (i.e. the 12 km simulations mapped to 60 km, WRF12-remap); P is the "target" (i.e. MODIS at 60 km) and output from WRF60 are used as the reference forecast; F' the difference between 12 km estimates regridded to 60 km and MODIS; P' the difference between the 60 km simulation and MODIS.

BSS measure ~~the improvement in the accuracy with which~~how much a test simulation (i.e. WRF12-remap) more closely (or poorly) reproduces observations (from MODIS, MERRA-2 or other satellite products) relative to a control (WRF60) run~~over output from WRF60~~. A BSS>0 indicates WRF12, even when regridded to 60 km, does add value. The first term in (4~~5~~) ranges from 0 to 1, is described as the potential skill, and is the square of the spatial correlation coefficient between forecast and reference anomalies to MODIS. It is the skill score achievable if both the conditional bias (second term) and overall bias (third term) were zero, and for most of the variables considered herein (particularly AOD) it contributes to a positive BSS in most calendar months (and seasons). The second term (the conditional bias, > 0), is the square of the difference between the anomaly correlation coefficient and the ratio of standard deviation of the anomalies and is small if for all points F' is linear to P'.~~.~~ The third term is referred to as the forecast anomaly bias, and is the ratio of the difference between the mean anomalies of WRF12-remap and the observations relative to WRF60 and the standard deviation of WRF60 anomaly relative to observed values. The fourth term is the degree of agreement and appears in both the numerator and denominator. It is computed as the square of the ratio of the mean anomaly between WRF60 and observations and the standard deviation of the anomalies.

(ii) Pooled paired t-test

To identify which areas in space contribute most to the added value, we compare daily mean AOD fields from WRF-Chem at different resolutions and MODIS. We perform a pooled paired t-test to evaluate the null hypothesis that those differences come from normal distributions with equal means and equal but unknown variances (the test statistic has a Student's *t* distribution with df = n + m – 2, and the sample standard deviation is the pooled standard deviation, where n and m are the two sample sizes). The test is conducted by climatological season (e.g. winter = DJF) since there are fewer than 20 valid AOD observations in most 60 km grid cells for each calendar month (Fig. 2). Given the large number of hypothesis tests performed (i.e. one for each 60 km grid cell), we adjust the p-values using the False Discovery Rate (FDR) approach (Benjamini and Hochberg, 1995). In this approach, p-values from the t-tests are ranked from low to high (p_1,p_2,…,p_m), then the test with the highest rank, *j*, satisfying:

$$p_j \le \frac{j}{m}\alpha \quad \textbf{(6)}$$

is identified. Here all p-values satisfying Eq. ~~5~~ 6 with α=0.1 are considered significant.

(iii) Accuracy and Hit Rate in identification of extremes

For each month we identify grid cells in which the wavelength specific AOD exceeds the 75th percentile value computed from all grid cells and define that as an extreme. Thus grid cells with extreme AOD are independently determined for MODIS and WRF-Chem at different resolutions. The spatial coherence in identification of extremes in the fields is quantified using two metrics: the *Accuracy* and the *Hit Rate* (*HR*). The *Accuracy* indicates the overall spatial coherence and is computed as the number of grid cells co-identified as extreme and non-extreme between WRF-Chem and MODIS relative to the total number of cells with valid data. The *HR* weights only correct identification of extremes in MODIS by WRF-Chem.

3 Results

3.1 Quantifying the value added of increased spatial resolution

When WRF-Chem is applied at 60 km resolution the degree of association of the resulting spatial fields of mean monthly AOD at the three wavelengths with MODIS varies seasonally. Smallest RMSD and highest Spearman spatial correlations (ρ) with MODIS observations generally occur during months with highest mean AOD (i.e. during summer, Fig. 1 d-f and Fig. 3), and reach a maximum in August (ρ = 0.60, Table 2~~Table 2~~~~Table 1~~). However, while the patterns of relative AOD variability are well captured, the absolute magnitudes and spatial gradients of AOD during the summer are underestimated by WRF60 (Fig. 1 d-f and Fig. 3, Table S~~2~~1). High spatial correlations (ρ > 0.40) are also observed in March, April and November (Table 2~~Table 2~~~~Table 1~~), when the ratio of spatial standard deviations is closer to 1 (Fig. 1 d-f, Table ~~S2~~S1). Only a weak wavelength dependence is observed in the performance metrics as described on Taylor diagrams. The spatial variability is generally more negatively biased for AOD at 660 nm (Table ~~S2~~S1), indicating that WRF60 simulations tend to produce larger diameter aerosols homogeneously distributed over the domain, whereas MODIS observations indicate more spatial variability.

The performance of WRF60 simulations relative to MODIS contrasts with analyses of WRF12 and WRF12-remap. WRF12 and WRF12-remap indicate highest spatial correlations with MODIS observations throughout the summer months (ρ = 0.5-0.7, Table 2~~Table 2~~~~Table 1~~), although the bias towards simulation of more coarse aerosols than are observed is consistent across the two simulations and with prior research (see details provided in (Crippa et al., 2016)). However, simulations at 12 km (WRF12) show positive ρ with MODIS for all λ in all calendar months, while mean monthly spatial fields of AOD from WRF60 show low

and/or negative correlations with MODIS during May, June, September, October and December, indicating substantial differences in the degree of correspondence with MODIS AOD in the two simulations, and higher fidelity of the enhanced resolution runs (Tables ~~1~~2 and S~~2~~1).

Monthly mean spatial fields of AOD(λ) as simulated by WRF12 or WRF12-remap exhibit positive Spearman correlation coefficients (ρ) with MODIS observations for all calendar months and range from ~ 0.25 for WRF12-remap (0.20 for WRF12) during winter to ~ 0.70 and 0.64, respectively during summer (Table 2~~Table 2~~~~Table 1~~). Spearman's ρ are uniformly higher in WRF12-remap than WRF12 indicating a mismatch in space in the high-resolution simulation (i.e. that grid cells with high AOD are slightly displaced in the 12 km simulations possibly due to the presence of sub-grid scale aerosol plumes (Rissman et al., 2013)). Mean monthly fields of AOD (all λ) from both WRF12 and WRF12-remap exhibit lower ρ with MODIS in February-April and November than the 60 km runs (Table 2~~Table 2~~~~Table 1~~). These discrepancies appear to be driven by conditions in the south of the domain. For example, differences between WRF60/WRF12-remap vs. MODIS during all seasons are significant according to the paired t-test over Florida and along most of the southern coastlines (Fig. 2). This region of significant differences extends up to ~ 40°N during summer and fall, reflecting the stronger north-south gradient in AOD from MODIS and WRF12-remap that is not captured by WRF60 (see example for λ = 550 nm, Fig. 3). These enhancements in the latitudinal gradients from WRF12-remap are also manifest in the physical variables (particularly specific humidity as discussed further below).

The differences in the absolute values of mean monthly AOD deriving from differences in the resolution at which WRF-Chem was applied are of sufficient magnitude (a difference of up to 0.2 in regions with a mean AOD value of 0.4), particularly in the summer months (Fig. 4), to raise concerns. However, detailed investigation of the simulations settings and repetition of the 60 km simulation resulted in virtually identical results indicating no fault can be found in the analysis. Further, we note ~~this is a region~~that the eastern-half of North America was also identified as a region of high discrepancy in global ESM (Myhre et al., 2013a).

To further investigate differences in the simulation output due to spatial discretization we computed Brier Skill Scores (BSS~~, Eq. 4~~). In this analysis AOD for each λ from WRF12-remap are used as the 'forecast', output from WRF60 are used as the reference forecast and MODIS observations at 60 km are used as the target. BSS exceed 0 during all months except

for September and October, and largest BSS (> 0.5) for AOD (all λ) is found during most months between December and July (Fig. 5). This indicates that running WRF-Chem at 12 km resolution adds value relative to WRF60, even when the WRF12 output is remapped to 60 km. BSS do not strongly depend on λ, indicating the added value from enhanced resolution similarly affects particles of different sizes. Inspecting the terms defining the BSS provides information about the origin of the added value (Fig. 5). The positive BSS derives principally from the potential skill (first term in Eq. ~~4~~5), which demonstrates a reduction in bias and/or more accurate representation of the spatial gradients in WRF12-remap. This term exhibits ~~a~~ weak seasonality with values below 0.5 only during August and fall months. The second and third terms are close to zero during most months, although bigger biases are found during August-October. The substantial conditional bias during late summer and early fall is the result of the large ratio of standard deviations (> 1, i.e. the spatial variability of the anomaly relative to MODIS is larger for WRF12-remap than WRF60, Table ~~S2~~S1). It thus contributes to the negative BSS found in September and October, which are also identified as outlier months in WRF12-remap from the Taylor diagram analysis (Fig. 1). Output for these months show modest spatial correlations with MODIS and higher ratio of standard deviations than in WRF60-MODIS comparisons (Fig. 1, Table ~~S2~~S1). Previous work ~~with analogous WRF-Chem settings~~ showed that the lower model skill (in WRF12) during September and October ~~can~~may be partially attributable to a dry bias in precipitation from WRF-Chem relative to observations. As a result, ~~a positive bias in~~ simulated AOD and near-surface aerosol nitrate and sulfate concentrations are positively biased ~~is present~~ over large ~~region~~parts of the domain (Crippa et al., 2016).

Model resolution also affects the *Accuracy* and *Hit Rate* (*HR*) for identification of areas of extreme AOD (AOD>75th percentile). Highest coherence in the identification of extreme AOD in space identified in WRF12-remap (and WRF12) relative to MODIS is found during May-August (*HR* = 53-77%) vs. WRF60 (*HR* = 17-54%, Table 3~~Table 2~~). Conversely highest *HR* are found for WRF60 and MODIS during winter and early spring, and indeed exceed those for WRF12 and WRF12-remap (Table 3~~Table 2~~, e.g. Feb: *HR* = 0.78 for WRF60, and 0.67 and 0.68 for WRF12 and WRF12-remap, respectively). These differences are consistent with the observation that WRF12-remap overestimates the scales of AOD coherence and AOD magnitude during the cold season along coastlines and over much of the domain in April (Fig. 3).

The synthesis of these analyses is thus that the higher resolution simulation increases the

overall spatial correlation, decreases overall bias in AOD close to the peak of the solar spectrum relative to MODIS observations and therefore the higher-resolution simulations better represent aerosol direct climate forcing. However, WRF12-remap exhibits little improvement over WRF60 in terms of reproducing the spatial variability of AOD ~~at these~~in the visible wavelengths and further that WRF12-remap tends to be more strongly positively biased in terms of mean monthly AOD outside of the summer months (Fig. 2 and Fig. 3). Also the improvement in detection of areas of extreme AOD in the higher resolution simulations (WRF12-remap) is manifest only during the warm season.

3.2 Investigating the origin of the added value and sources of error in simulated AOD

As documented above, WRF-Chem applied at either 60 or 12 km resolution over eastern North America exhibits some skill in reproducing observed spatial fields of AOD and the occurrence of extreme AOD values. However, marked discrepancies both in space and time are found, and at least some of them show a significant dependence on model resolution. Thus, we investigated a range of physical conditions and gas phase concentrations known to be strongly determinant of aerosol dynamics in terms of the BSS as a function of model resolution and also in terms of the mean monthly spatial patterns.

WRF12 even when remapped to 60 km provides more accurate description of key meteorological variables such as specific humidity (Q) within the boundary layer, *PBLH*, surface temperature and precipitation (Fig. 6, S1, S2 and S3) when ~~comparing~~ compared to MERRA-2, as indicated by the positive BSS during almost all months (Fig. 7a). Good qualitative agreement is observed for the spatial patterns and absolute magnitude of T_{2m} in both WRF60 and WRF12-remap relative to MERRA-2 for all seasons (Fig. S1) leading to only modest magnitude of BSS (i.e. value added by the higher resolution simulations (Fig. 7a)). The aerosol size distribution and therefore wavelength specific AOD exhibits a strong sensitivity to Q (Santarpia et al., 2005) due to the presence of hygroscopic components in atmospheric aerosols and thus the role of water uptake in determining aerosol diameter, refractivity and extinction coefficient (Zieger et al., 2013). For example, the hygroscopic growth factor, which indicates the change of aerosol diameter due to water uptake, is ~ 1.4 for pure ammonium sulfate with dry diameter of 532 nm at relative humidity of 80%, thus biases in representation atmospheric humidity may lead to big errors in simulated aerosol size and AOD (Flores et al., 2012). Our previous analyses of the 12 km resolution simulations indicated overestimation of sulfate aerosols (a highly hygroscopic aerosol component, and

one which in many chemical forms exhibits strong hysteresis (Martin et al., 2004)) relative to observed near-surface $PM_{2.5}$ concentrations during all seasons except for winter (Crippa et al., 2016), leading to the hypothesis that simulated AOD and discrepancies therein may exhibit a strong dependence on *Q*. Consistent with that postulate, Q_{PBL} from WRF12-remap exhibits a ~~wet~~ moist bias in cloud-free grid cells mostly during warm months, whereas WRF60 is characterized by a dry bias during all seasons (Fig. 6). Despite the positive bias, WRF12-remap better captures the seasonal spatial patterns of Q_{PBL} in MERRA-2, leading to positive BSS in all calendar months. Thus, there is added value by higher-resolution simulations in representation of one of the key parameters dictating particle growth and optical properties. Spatial patterns of differences in Q_{PBL} from WRF60 and WRF12-remap relative to MERRA-2 (Fig. 6) exhibit similarities to differences in AOD (Fig. 4). WRF60 is dry-biased relative to WRF12 particularly during the summer (and fall) and underestimates Q_{PBL} relative to MERRA-2 during all seasons over the southern states and over most of continental US during summer and fall. Conversely, WRF12-remap overestimates Q_{PBL} over most of continental US during summer and fall relative to MERRA-2.

PBLH is a key variable for dictating near-surface aerosol concentrations but is highly sensitive to the physical schemes applied, and biases appear to be domain and resolution dependent. However, this parameter is comparatively difficult to assess because differences in *PBLH* ~~PBL heights between~~from WRF-Chem and MERRA-2 may also originate from the way they are computed (i.e. from heat diffusivity in MERRA-2 (Jordan et al., 2010) and from turbulent kinetic energy in WRF-Chem (Janjić, 2002;von Engeln and Teixeira, 2013)~~)~~). Nevertheless, t~~TFor example, t~~he Mellor-Yamada-Janjich *PBL* scheme combined with the Noah Land Surface Model applied in this work was found to produce lower *PBL* heights (Zhang et al., 2009) than other parameterizations. ~~(Jordan et al., 2010)(Janjić, 2002)(von Engeln and Teixeira, 2013)~~ Thus, the positive bias in simulated AOD and surface $PM_{2.5}$ concentrations (reported previously in (Crippa et al., 2016)) may be linked to the systematic underestimation of *PBLH* simulated by WRF12-remap over continental US relative to MERRA-2 during all seasons (except winter) with greatest bias over regions of complex topography (Fig. S2). ~~However, a~~A positive bias (of several hundred meters) in terms of *PBLH* for WRF simulations using the MYJ parameterization was previously reported for high-resolution simulations over complex terrain (Rissman et al., 2013), and a positive bias in *PBLH* is also observed in the 60 km simulations presented herein (Fig. S2). This may provide a partial~~ly~~ explanation for the strong negative bias in AOD in WRF60 during summer (Fig.

3). In general, the BSS indicate improvement in the simulation of *PBLH* in WRF12-remap than in WRF60 (Fig. 7a).

Consistent with the dry bias in Q_{PBL} in WRF60, total accumulated precipitation is also underestimated in WRF60, while WRF12-remap captures the absolute magnitudes and the spatial patterns therein (Fig. S3). Analysis of hourly precipitation rates also showed higher skill of WRF12-remap than WRF60 in correctly simulating precipitation occurrence (*HR*) relative to MERRA-2 (Table S~~3~~2). More specifically WRF12-remap correctly predicts between 40% and 70 % of precipitation events in MERRA-2 with highest skill during winter months, whereas WRF60 output exhibits lower HR (~6% during summer and 30% during winter). This result thus confirms our expectation of a strong sensitivity of model performance to resolution due to the inherent scale dependence in the cumulus scheme.

Gas phase concentrations (transformed into z-scores) from WRF12-remap show higher agreement with satellite observations during almost all months, as indicated by the positive BSS (Fig. 7b). However given the limited availability of valid satellite observations (especially during months with low radiation intensity), the BSS are likely only robust for the summer months for all species. Nevertheless, with the exception of NH_3 during June, BSS for all months are above or close to zero indicating that on average, the enhanced resolution simulations do improve the quality of the simulation of the gas phase species even when remapped to 60 km resolution. Further, the seasonal average spatial patterns of the total columnar concentrations, expressed in terms of z-scores, also exhibit ~~high~~ qualitative agreement with the satellite observations (Fig. S4-S7).

4 Concluding remarks

This analysis is one of the first to quantify the impact of model spatial resolution on the spatio-temporal variability and magnitude of AOD, and does so using simulations for a full calendar year. Application of WRF-Chem at two different resolutions (60 km and 12 km) over eastern North America for a representative year (2008) leads to the following conclusions:

- Higher resolution simulations add value (i.e. enhance the fidelity of AOD at and near to the peak in the solar spectrum) relative to a coarser run, although the improvement in model performance is not uniform in space and time. Brier Skill Scores for the remapped simulations (i.e. output from simulations conducted at 12 km (WRF12) then averaged to 60 km, WRF12-remap) are positive for ten of twelve calendar moths,

and for AOD(λ=550 nm) exceed 0.5 for seven of twelve months.

- Spatial correlations of output from WRF12 and WRF12-remap with observations from MODIS are higher than output from a simulation conducted at 60 km during most months. For example, in contrast to WRF-Chem simulations at 60 km (WRF60), simulations conducted at 12 km (WRF12) show positive spatial correlations with MODIS for all λ in all calendar months, and particularly during summer (ρ = 0.5-0.7).
- Output from WRF12 and WRF12-remap exhibit highest accord with MODIS observations in capturing the frequency, magnitude and location of extreme AOD values during summer when AOD is typically highest. During May-August WRF12-remap has *Hit Rates* for identification of extreme AOD of 53-78%.
- At least some of the improvement in the accuracy with which AOD is reproduced in the higher resolution simulations may be due to improved fidelity of specific humidity and thus more accurate representation of hygroscopic growth of some aerosol components.
- Higher-resolution simulations also add value in the representation of other key meteorological variables such as temperature, boundary layer height and precipitation. Both spatial patterns and precipitation occurrence are better captured by WRF12-remap.
- More accurate representation of spatial patterns and magnitude of gaseous species that play~~ing~~ a key role in particle formation and growth is also achieved by running WRF-Chem at high resolution.

It is worthy of note that even the 12 km resolution WRF-Chem simulations exhibit substantial differences in AOD relative to MODIS over eastern North America, and the agreement varies only slightly with wavelength. This may be partially attributable to use of the modal approach to represent the aerosol size distribution in order to enhance computational tractability. In this application each mode has a fixed geometric standard deviation (σ_g), which can lead to biases in simulated AOD in the visible wavelengths by up to 25% (Brock et al., 2016) (with the model overestimating observations if the prescribed σ_g is larger than the observed one). Setting σ_g = 2 for the accumulation mode (the default in WRF-Chem) may lead to an overestimation of the number of particles at the end of the accumulation mode tail, and there is evidence that a value of $\sigma_{g,acc}$=1.40 leads to higher agreement with observations (Mann et al., 2012). Further possible sources of the AOD biases reported herein derive from selection of the physical schemes (e.g. planetary boundary layer (*PBL*) schemes and land-surface

model (Misenis and Zhang, 2010;Zhang et al., 2009)). Further, it is worth mentioning that NEI emissions are specified based on an average summertime weekday, so ~~higher~~ enhanced model performance might be achieved if seasonally varying emissions ~~would be~~were available. Future work will include a systematic sensitivity analysis of these effects.

Acknowledgments

This research was supported in part by a L'Oréal-UNESCO UK and Ireland Fellowship For Women In Science (to PC), the Natural Environmental Research Council (NERC) through the LICS project (ref. NE/K010794/1), grants to SCP from US NSF (grant~~s~~ # ~~1102309 and~~ 1517365) and NASA (NNX16AG31G~~under NRA NNH14ZDA001N~~), and a NASA Earth and Space Science Fellowship Program - Grant "14-EARTH14F-0207" (to RCS). Further support was provided by the Lilly Endowment, Inc., through its support for the Indiana University Pervasive Technology Institute and the Indiana METACyt Initiative. We gratefully acknowledge the NASA scientists responsible for MERRA-2 and MODIS products, the developers of WRF-Chem, and Lieven Clarisse, Simon Whitburn, and Martin Van Damme for producing and sharing the NH_3 retrievals.

References

Ackermann, I. J., Hass, H., Memmesheimer, M., Ebel, A., Binkowski, F. S., and Shankar, U.: Modal aerosol dynamics model for Europe: development and first applications, Atmos. Environ., 32, 2981-2999, http://dx.doi.org/10.1016/S1352-2310(98)00006-5, 1998.

Anderson, T. L., Charlson, R. J., Winker, D. M., Ogren, J. A., and Holmén, K.: Mesoscale Variations of Tropospheric Aerosols, Journal of the Atmospheric Sciences, 60, 119-136, doi: http://dx.doi.org/10.1175/1520-0469(2003)060<0119:MVOTA>2.0.CO;2, 2003.

Ångström, A.: The parameters of atmospheric turbidity, Tellus, 16, 64-75, 10.1111/j.2153-3490.1964.tb00144.x, 1964.

Benjamini, Y., and Hochberg, Y.: Controlling the False Discovery Rate: A Practical and Powerful Approach to Multiple Testing, Journal of the Royal Statistical Society. Series B (Methodological), 57, 289-300, 1995.

Boucher, O., D. Randall, P. Artaxo, C. Bretherton, G. Feingold, P. Forster, V.-M. Kerminen, Y. Kondo, H. Liao, U. Lohmann, P. Rasch, S.K. Satheesh, S. Sherwood, B. Stevens and X.Y. Zhang: Clouds and Aerosols, in: Climate Change 2013: The Physical Science Basis. Contribution of Working Group I to the Fifth Assessment Report of the Intergovernmental Panel on Climate Change, edited by: Stocker, T. F., D. Qin, G.-K. Plattner, M. Tignor, S.K. Allen, J. Boschung, A. Nauels, Y. Xia, V. Bex and P.M. Midgley, Cambridge University Press, Cambridge, United Kingdom and New York, NY, USA, 33–115, 2013.

Brinksma, E. J., K. F. Boersma, P. F. Levelt, and R. D. McPeters OMI validation requirements document, Version 1, Rep. RS-OMIE-KNMI-345, 66, 2003.

Brock, C. A., Wagner, N. L., Anderson, B. E., Attwood, A. R., Beyersdorf, A., Campuzano-Jost, P., Carlton, A. G., Day, D. A., Diskin, G. S., Gordon, T. D., Jimenez, J. L., Lack, D. A., Liao, J., Markovic, M. Z., Middlebrook, A. M., Ng, N. L., Perring, A. E., Richardson, M. S., Schwarz, J. P., Washenfelder, R. A., Welti, A., Xu, L., Ziemba, L. D., and Murphy, D. M.: Aerosol optical properties in the southeastern United States in summer – Part 1: Hygroscopic growth, Atmos. Chem. Phys., 16, 25695-25738, doi:10.5194/acp-16-5009-2016, 2016.

Chance, K.: OMI algorithm theoretical basis document, volume IV: OMI trace gas algorithms, 2002.

Chen, F., and Dudhia, J.: Coupling an advanced land surface–hydrology model with the Penn State–NCAR MM5 modeling system. Part I: model implementation and sensitivity, Monthly Weather Review, 129, 569-585, doi:10.1175/1520-0493(2001)129<0569:CAALSH>2.0.CO;2, 2001.

Chin, M., Kahn, R. A., and Schwartz , S. E.: Atmospheric Aerosols Properties and Climate Impacts. A Report by the U.S. Climate Change Science Program and the Subcommittee on Global Change Research, in, National Aeronautics and Space Administration, Washington, D.C., USA, 128, 2009.

Crippa, P., Sullivan, R. C., Thota, A., and Pryor, S. C.: Evaluating the skill of high-resolution WRF-Chem simulations in describing drivers of aerosol direct climate forcing on the regional scale, Atmos. Chem. Phys., 16, 397-416, 10.5194/acp-16-397-2016, 2016.

Di Luca, A., de Elía, R., and Laprise, R.: Challenges in the Quest for Added Value of Regional Climate Dynamical Downscaling, Curr Clim Change Rep, 1, 10-21, 10.1007/s40641-015-0003-9, 2015.

Diaconescu, E., and Laprise, R.: Can added value be expected in RCM-simulated large scales?, Clim Dyn, 41, 1769-1800, 10.1007/s00382-012-1649-9, 2013.

Emmons, L. K., Walters, S., Hess, P. G., Lamarque, J. F., Pfister, G. G., Fillmore, D., Granier, C., Guenther, A., Kinnison, D., Laepple, T., Orlando, J., Tie, X., Tyndall, G., Wiedinmyer, C., Baughcum, S. L., and Kloster, S.: Description and evaluation of the Model for Ozone and Related chemical Tracers, version 4 (MOZART-4), Geoscientific Model Development, 3, 43-67, doi:10.5194/gmd-3-43-2010, 2010.

Fast, J. D., Gustafson, W. I., Easter, R. C., Zaveri, R. A., Barnard, J. C., Chapman, E. G., Grell, G. A., and Peckham, S. E.: Evolution of ozone, particulates, and aerosol direct radiative forcing in the vicinity of Houston using a fully coupled meteorology-chemistry-aerosol model, Journal of Geophysical Research: Atmospheres, 111, D21305, 10.1029/2005JD006721, 2006.

Fioletov, V. E., McLinden, C. A., Krotkov, N., Moran, M. D., and Yang, K.: Estimation of SO_2 emissions using OMI retrievals, Geophysical Research Letters, 38, L21811, 10.1029/2011GL049402, 2011.

Flores, J. M., Bar-Or, R. Z., Bluvshtein, N., Abo-Riziq, A., Kostinski, A., Borrmann, S., Koren, I., Koren, I., and Rudich, Y.: Absorbing aerosols at high relative humidity: linking

615 hygroscopic growth to optical properties, Atmospheric Chemistry and Physics, 12, 5511-
616 5521, 10.5194/acp-12-5511-2012, 2012.

617 Grell, G. A., and Dévényi, D.: A generalized approach to parameterizing convection
618 combining ensemble and data assimilation techniques, Geophysical Research Letters, 29, 38-
619 31-38-34, 10.1029/2002GL015311, 2002.

620 Grell, G. A., Peckham, S. E., Schmitz, R., McKeen, S. A., Frost, G., Skamarock, W. C., and
621 Eder, B.: Fully coupled "online" chemistry within the WRF model, Atmos. Environ., 39,
622 6957-6975, 10.1016/j.atmosenv.2005.04.027, 2005.

623 Guenther, A., Zimmerman, P., and Wildermuth, M.: Natural volatile organic compound
624 emission rate estimates for U.S. woodland landscapes, Atmos. Environ., 28, 1197-1210,
625 10.1016/1352-2310(94)90297-6, 1994.

626 Guenther, A. B., Zimmerman, P. R., Harley, P. C., Monson, R. K., and Fall, R.: Isoprene and
627 monoterpene emission rate variability: model evaluations and sensitivity analyses, J.
628 Geophys. Res.-Atmos., 98, 12609-12617, 10.1029/93jd00527, 1993.

629 Gustafson, W. I., Qian, Y., and Fast, J. D.: Downscaling aerosols and the impact of neglected
630 subgrid processes on direct aerosol radiative forcing for a representative global climate model
631 grid spacing, Journal of Geophysical Research: Atmospheres, 116, D13303,
632 10.1029/2010JD015480, 2011.

633 Hong, S.-Y., Dudhia, J., and Chen, S.-H.: A Revised Approach to Ice Microphysical
634 Processes for the Bulk Parameterization of Clouds and Precipitation, Monthly Weather
635 Review, 132, 103-120, doi:10.1175/1520-0493(2004)132<0103:ARATIM>2.0.CO;2, 2004.

636 Hyer, E. J., Reid, J. S., and Zhang, J.: An over-land aerosol optical depth data set for data
637 assimilation by filtering, correction, and aggregation of MODIS Collection 5 optical depth
638 retrievals, Atmospheric Measurement Techniques, 4, 379-408, 10.5194/amt-4-379-2011,
639 2011.

640 Janjić, Z. I.: The Step-Mountain Eta Coordinate Model: Further Developments of the
641 Convection, Viscous Sublayer, and Turbulence Closure Schemes, Monthly Weather Review,
642 122, 927-945, doi:10.1175/1520-0493(1994)122<0927:TSMECM>2.0.CO;2, 1994.

643 Janjić, Z. I.: Nonsingular implementation of the Mellor–Yamada level 2.5 scheme in the
644 NCEP Meso model, NCEP office note, 437, 61, 2002.

645 Jordan, N. S., Hoff, R. M., and Bacmeister, J. T.: Validation of Goddard Earth Observing
646 System-version 5 MERRA planetary boundary layer heights using CALIPSO, J. Geophys.
647 Res.-Atmos., 115, 10.1029/2009jd013777, 2010.

648 Krotkov, N. A., McClure, B., Dickerson, R. R., Carn, S. A., Li, C., Bhartia, P. K., Yang, K.,
649 Krueger, A. J., Li, Z., Levelt, P. F., Chen, H., Wang, P., and Lu, D.: Validation of SO_2
650 retrievals from the Ozone Monitoring Instrument over NE China, Journal of Geophysical
651 Research: Atmospheres, 113, D16S40, 10.1029/2007JD008818, 2008.

652 Leibensperger, E., Mickley, L. J., Jacob, D. J., Chen, W.-T., Seinfeld, J., Nenes, A., Adams,
653 P., Streets, D., Kumar, N., and Rind, D.: Climatic effects of 1950–2050 changes in US

anthropogenic aerosols–Part 1: Aerosol trends and radiative forcing, Atmospheric Chemistry and Physics, 12, 3333-3348, doi:10.5194/acp-12-3333-2012, 2012.

Levy, R. C., Mattoo, S., Munchak, L. A., Remer, L. A., Sayer, A. M., Patadia, F., and Hsu, N. C.: The Collection 6 MODIS aerosol products over land and ocean, Atmospheric Measurement Techniques, 6, 2989-3034, 10.5194/amt-6-2989-2013, 2013.

Long, M., Yantosca, R., Nielsen, J., Keller, C., da Silva, A., Sulprizio, M., Pawson, S., and Jacob, D.: Development of a grid-independent GEOS-Chem chemical transport model (v9-02) as an atmospheric chemistry module for Earth system models, Geoscientific Model Development, 8, 595-602, doi:10.5194/gmd-8-595-2015, 2015.

Mann, G. W., Carslaw, K. S., Ridley, D. A., Spracklen, D. V., Pringle, K. J., Merikanto, J., Korhonen, H., Schwarz, J. P., Lee, L. A., Manktelow, P. T., Woodhouse, M. T., Schmidt, A., Breider, T. J., Emmerson, K. M., Reddington, C. L., Chipperfield, M. P., and Pickering, S. J.: Intercomparison of modal and sectional aerosol microphysics representations within the same 3-D global chemical transport model, Atmospheric Chemistry and Physics, 12, 4449-4476, 10.5194/acp-12-4449-2012, 2012.

Martin, S. T., Hung, H. M., Park, R. J., Jacob, D. J., Spurr, R. J. D., Chance, K. V., and Chin, M.: Effects of the physical state of tropospheric ammonium-sulfate-nitrate particles on global aerosol direct radiative forcing, Atmospheric Chemistry and Physics, 4, 183-214, doi:10.5194/acp-4-183-2004, 2004.

McComiskey, A., Schwartz, S. E., Schmid, B., Guan, H., Lewis, E. R., Ricchiazzi, P., and Ogren, J. A.: Direct aerosol forcing: Calculation from observables and sensitivities to inputs, Journal of Geophysical Research: Atmospheres, 113, D09202, 10.1029/2007JD009170, 2008.

McLinden, C. A., Fioletov, V., Boersma, K. F., Kharol, S. K., Krotkov, N., Lamsal, L., Makar, P. A., Martin, R. V., Veefkind, J. P., and Yang, K.: Improved satellite retrievals of NO_2 and SO_2 over the Canadian oil sands and comparisons with surface measurements, Atmos. Chem. Phys., 14, 3637-3656, 10.5194/acp-14-3637-2014, 2014.

Meehl, G. A., Moss, R., Taylor, K. A., Eyring, V., Stouffer, R. J., Sandrine, B., and Stevens, B.: Climate model intercomparisons: preparing for the next phase, Eos, Transaction, American Geophysical Union, 95, 77-84, doi:10.1002/2014EO09, 2014.

Misenis, C., and Zhang, Y.: An examination of sensitivity of WRF/Chem predictions to physical parameterizations, horizontal grid spacing, and nesting options, Atmospheric Research, 97, 315-334, 10.1016/j.atmosres.2010.04.005, 2010.

Mlawer, E. J., Taubman, S. J., Brown, P. D., Iacono, M. J., and Clough, S. A.: Radiative transfer for inhomogeneous atmospheres: RRTM, a validated correlated-k model for the longwave, Journal of Geophysical Research: Atmospheres, 102, 16663-16682, 10.1029/97JD00237, 1997.

Molod, A., Takacs, L., Suarez, M., and Bacmeister, J.: Development of the GEOS-5 atmospheric general circulation model: evolution from MERRA to MERRA2, Geoscientific Model Development, 8, 1339-1356, 10.5194/gmd-8-1339-2015, 2015.

693 Murphy, A. H., and Epstein, E. S.: Skill scores and correlation-coefficients in model
694 verification, Monthly Weather Review, 117, 572-581, 10.1175/1520-
695 0493(1989)117<0572:ssacci>2.0.co;2, 1989.

696 Myhre, G., Samset, B. H., Schulz, M., Balkanski, Y., Bauer, S., Berntsen, T. K., Bian, H.,
697 Bellouin, N., Chin, M., Diehl, T., Easter, R. C., Feichter, J., Ghan, S. J., Hauglustaine, D.,
698 Iversen, T., Kinne, S., Kirkevag, A., Lamarque, J. F., Lin, G., Liu, X., Lund, M. T., Luo, G.,
699 Ma, X., van Noije, T., Penner, J. E., Rasch, P. J., Ruiz, A., Seland, O., Skeie, R. B., Stier, P.,
700 Takemura, T., Tsigaridis, K., Wang, P., Wang, Z., Xu, L., Yu, H., Yu, F., Yoon, J. H., Zhang,
701 K., Zhang, H., and Zhou, C.: Radiative forcing of the direct aerosol effect from AeroCom
702 Phase II simulations, Atmospheric Chemistry and Physics, 13, 1853-1877, 10.5194/acp-13-
703 1853-2013, 2013a.

704 Myhre, G., Shindell, D., Bréon, F.-M., Collins, W., Fuglestvedt, J., Huang, J., Koch, D.,
705 Lamarque, J.-F., Lee, D., Mendoza, B., Nakajima, T., Robock, A., Stephens, G., Takemura,
706 T., and Zhang, H.: Anthropogenic and Natural Radiative Forcing, in: Climate Change 2013:
707 The Physical Science Basis. Contribution of Working Group I to the Fifth Assessment Report
708 of the Intergovernmental Panel on Climate Change, edited by: Stocker, T. F., Qin, D.,
709 Plattner, G.-K., Tignor, M., Allen, S. K., Boschung, J., Nauels, A., Xia, Y., Bex, V., and
710 Midgley, P. M., Cambridge University Press, Cambridge, United Kingdom and New York,
711 NY, USA, 659–740, 2013b.

712 Qian, Y., Gustafson Jr, W. I., and Fast, J. D.: An investigation of the sub-grid variability of
713 trace gases and aerosols for global climate modeling, Atmos. Chem. Phys., 10, 6917-6946,
714 10.5194/acp-10-6917-2010, 2010.

715 Rissman, J., Arunachalam, S., Woody, M., West, J. J., BenDor, T., and Binkowski, F. S.: A
716 plume-in-grid approach to characterize air quality impacts of aircraft emissions at the
717 Hartsfield–Jackson Atlanta International Airport, Atmos. Chem. Phys., 13, 9285-9302,
718 10.5194/acp-13-9285-2013, 2013.

719 Rockel, B., Castro, C. L., Pielke, R. A., von Storch, H., and Leoncini, G.: Dynamical
720 downscaling: Assessment of model system dependent retained and added variability for two
721 different regional climate models, Journal of Geophysical Research: Atmospheres, 113,
722 D21107, 10.1029/2007JD009461, 2008.

723 Santarpia, J. L., Gasparini, R., Li, R. J., and Collins, D. R.: Diurnal variations in the
724 hygroscopic growth cycles of ambient aerosol populations, J. Geophys. Res.-Atmos., 110,
725 10.1029/2004jd005279, 2005.

726 Schell, B., Ackermann, I. J., Hass, H., Binkowski, F. S., and Ebel, A.: Modeling the
727 formation of secondary organic aerosol within a comprehensive air quality model system, J.
728 Geophys. Res.-Atmos., 106, 28275-28293, 10.1029/2001jd000384, 2001.

729 Schuster, G. L., O. Dubovik, and B. N. Holben Angstrom exponent and bimodal aerosol size
730 distributions, J. Geophys. Res.-Atmos., 111, D07207, doi:10.1029/2005JD006328., 2006.

731 Seinfeld, J. H., and Pandis, S. N.: Atmospheric chemistry and physics: from air pollution to
732 climate change, John Wiley & Sons, 1152 pp., 2016.

Simes, R. J.: An improved Bonferroni procedure for multiple tests of significance, Biometrika, 73, 751-754, 10.2307/2336545, 1986.

Simpson, D., Guenther, A., Hewitt, C. N., and Steinbrecher, R.: Biogenic emissions in Europe. 1. estimates and uncertainties, J. Geophys. Res.-Atmos., 100, 22875-22890, 10.1029/95jd02368, 1995.

Stocker, T. F. a. Q., D. and Plattner, G.-K. and Alexander, L.V. and Allen, S.K. and Bindoff, N.L. and Bréon, F.-M. and Church, J.A. and Cubasch, U. and Emori, S. and Forster, P. and Friedlingstein, P. and Gillett, N. and Gregory, J.M. and Hartmann, D.L. and Jansen, E. and Kirtman, B. and Knutti, R. and Krishna Kumar, K. and Lemke, P. and Marotzke, J. and Masson-Delmotte, V. and Meehl, G.A. and Mokhov, I.I. and Piao, S. and Ramaswamy, V. and Randall, D. and Rhein, M. and Rojas, M. and Sabine, C. and Shindell, D. and Talley, L.D. and Vaughan, D.G. and Xie, S.-P.: Summary for Policymakers, in: Climate Change 2013: The Physical Science Basis. Contribution of Working Group I to the Fifth Assessment Report of the Intergovernmental Panel on Climate Change, Cambridge University Press, Cambridge, United Kingdom and New York, NY, USA, 33–115, 2013.

Stockwell, W. R., Middleton, P., Chang, J. S., and Tang, X.: The second generation regional acid deposition model chemical mechanism for regional air quality modeling, Journal of Geophysical Research: Atmospheres, 95, 16343-16367, 10.1029/JD095iD10p16343, 1990.

Taylor, K. E.: Summarizing multiple aspects of model performance in a single diagram, J. Geophys. Res.-Atmos., 106, 7183-7192, 10.1029/2000jd900719, 2001.

Tilmes, S., Lamarque, J.-F., Emmons, L., Kinnison, D., Ma, P.-L., Liu, X., Ghan, S., Bardeen, C., Arnold, S., and Deeter, M.: Description and evaluation of tropospheric chemistry and aerosols in the Community Earth System Model (CESM1. 2), Geoscientific Model Development, 8, 1395-1426, doi:10.5194/gmd-8-1395-2015, 2015.

Tomasi, C., Caroli, E., and Vitale, V.: Study of the Relationship between Ångström's Wavelength Exponent and Junge Particle Size Distribution Exponent, Journal of Climate and Applied Meteorology, 22, 1707-1716, 10.1175/1520-0450(1983)022<1707:SOTRBW>2.0.CO;2, 1983.

US-EPA: 2005 National Emissions Inventory (NEI), US Environmental Protection Agency in, available at: ftp://aftp.fsl.noaa.gov/divisions/taq/emissions_data_2005/, 2009.

Vinken, G. C. M., Boersma, K. F., van Donkelaar, A., and Zhang, L.: Constraints on ship NO_x emissions in Europe using GEOS-Chem and OMI satellite NO_2 observations, Atmos. Chem. Phys., 14, 1353-1369, 10.5194/acp-14-1353-2014, 2014.

von Engeln, A., and Teixeira, J.: A Planetary Boundary Layer Height Climatology Derived from ECMWF Reanalysis Data, Journal of Climate, 26, 6575–6590, doi: 10.1175/JCLI-D-12-00385.1, 2013.

Weigum, N., Schutgens, N., and Stier, P.: Effect of aerosol sub-grid variability on aerosol optical depth and cloud condensation nuclei: Implications for global aerosol modelling, Atmos. Chem. Phys. Discuss., 2016, 1-36, 10.5194/acp-2016-360, 2016.

Whitburn, S., Van Damme, M., Clarisse, L., Bauduin, S., Heald, C., Hadji-Lazaro, J., Hurtmans, D., Zondlo, M. A., Clerbaux, C., Coheur, P.-F. : A flexible and robust neural

774 network IASI-NH_3 retrieval algorithm, J. Geophys. Res. Atmos, In Press,
775 10.1002/2016JD024828, 2016.

776 Wild, O., Zhu, X., and Prather, M. J.: Fast-J: Accurate Simulation of In- and Below-Cloud
777 Photolysis in Tropospheric Chemical Models, Journal of Atmospheric Chemistry, 37, 245-
778 282, 10.1023/a:1006415919030, 2000.

779 Zhang, Y., Dubey, M. K., Olsen, S. C., Zheng, J., and Zhang, R.: Comparisons of
780 WRF/Chem simulations in Mexico City with ground-based RAMA measurements during the
781 2006-MILAGRO, Atmospheric Chemistry and Physics, 9, 3777-3798, doi:10.5194/acp-9-
782 3777-2009, 2009.

783 Zieger, P., Fierz-Schmidhauser, R., Weingartner, E., and Baltensperger, U.: Effects of
784 relative humidity on aerosol light scattering: results from different European sites,
785 Atmospheric Chemistry and Physics, 13, 10609-10631, 10.5194/acp-13-10609-2013, 2013.

786

787

Figures

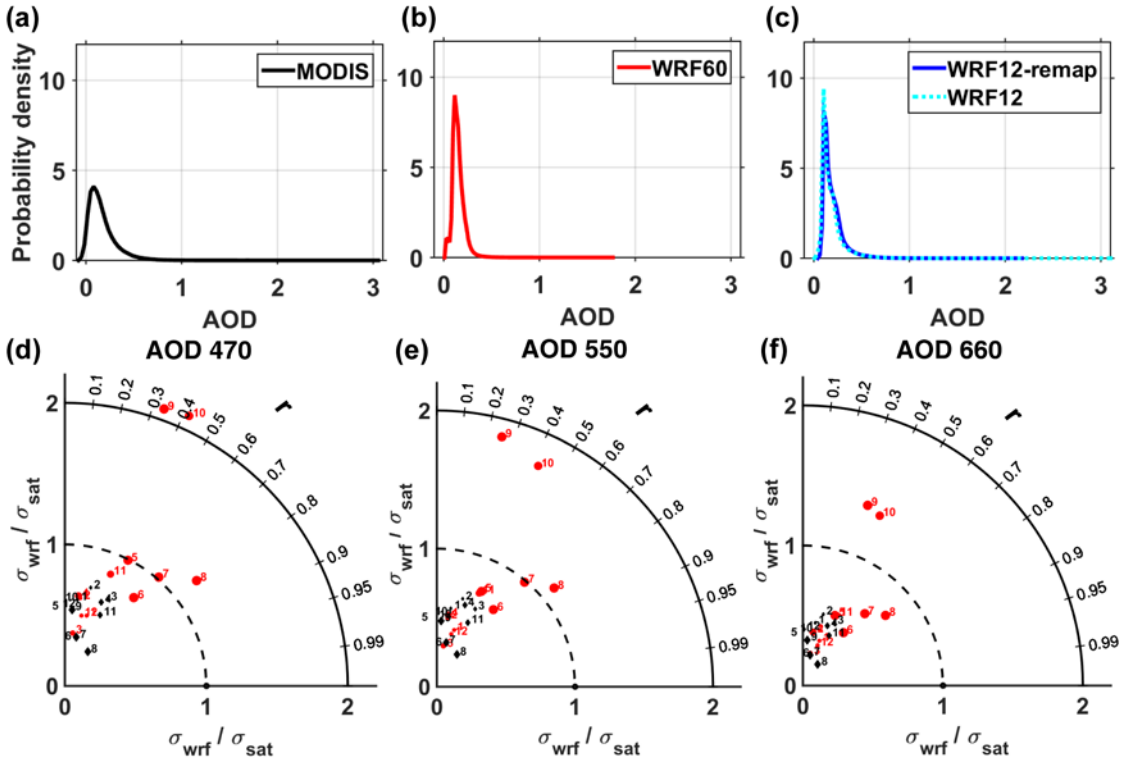

Figure 1. Probability density function of once daily AOD at a wavelength (λ) of 550 nm for (a) MODIS, (b) WRF60 and (c) WRF12 and WRF12-remap during the year 2008. (d-f) Taylor diagrams of mean monthly AOD at wavelengths (λ) of (d) 470, (e) 550 and (f) 660 nm as simulated by WRF-Chem at different resolutions (black diamonds=WRF60 and red dots=WRF12-remap) relative to MODIS observations. The numbers by each symbol denote the calendar month (e.g. 1=January).

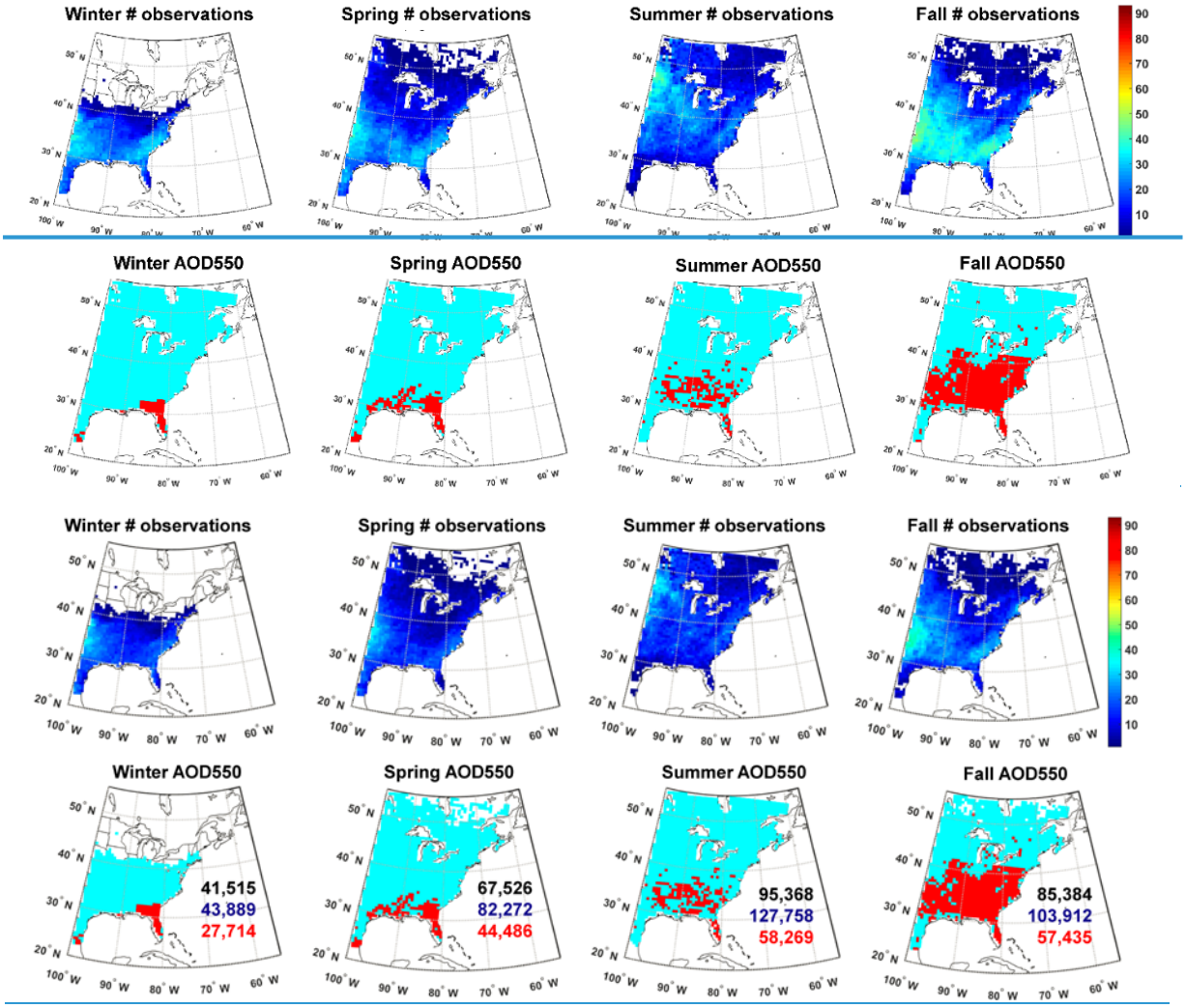

Figure 2. First line: Number of paired AOD observations at a wavelength (λ) of 550 nm (i.e. simultaneous values as output from WRF-Chem and observed by MODIS) used to perform a t-test designed to evaluate whether the difference computed for each grid cell as WRF60-MODIS differs from that computed as WRF12-remap-MODIS on a seasonal basis (columns show Winter (DJF), Spring (MAM), Summer (JJA) and Fall (SON)). Second line: Results of the t-test. Pixels that have p-values that are significantly different at α=0.10 are indicated in red and have been corrected for multiple testing using a False Discovery Rate approach. The number of observations of cloud-free conditions summed across all days in each season and all grid cells is also reported (black=MODIS, blue=WRF60, red=WRF12-remap).

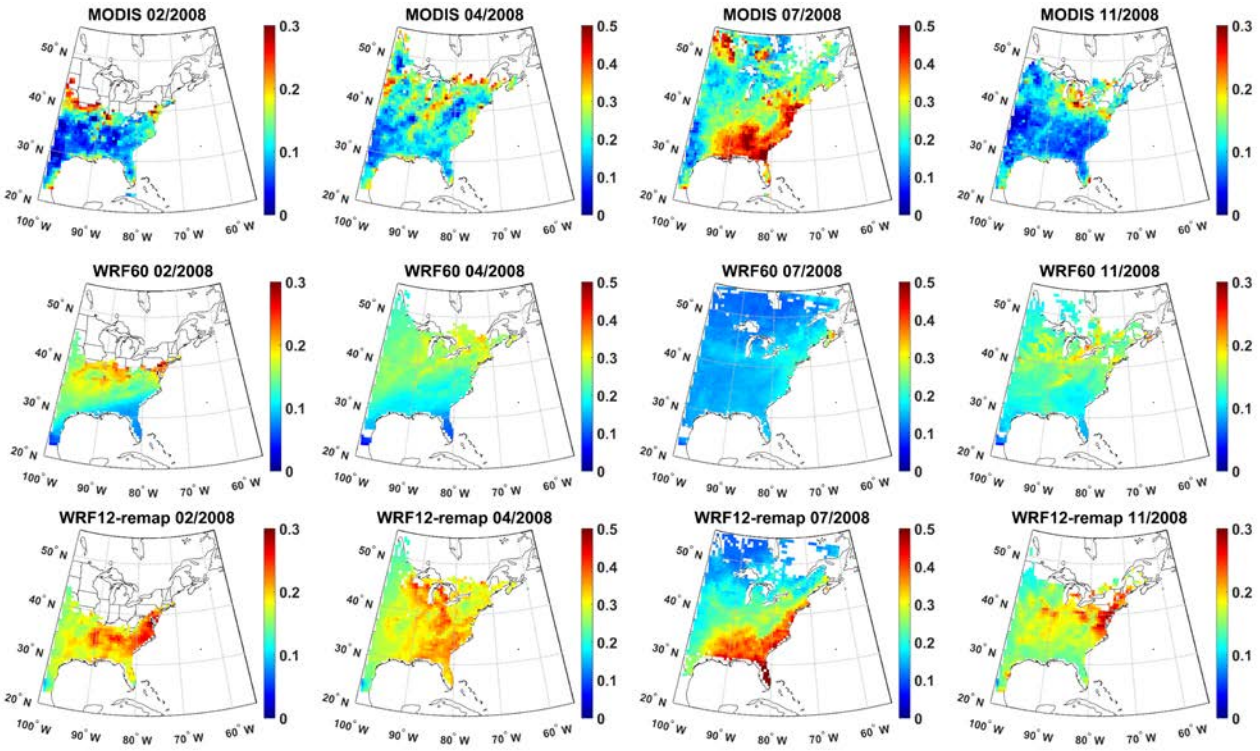

Figure 3. Monthly mean AOD at a wavelength (λ) of 550 nm from MODIS (first line) and WRF-Chem at different resolutions (WRF60 and WRF12-remap, second and third line) during a representative month in each climatological season (columns). Note that a different color scale is applied for different months. For a monthly mean value for a grid cell to be shown, there must be at least 5-simultaneous daily values (for the time of the satellite overpass) available.

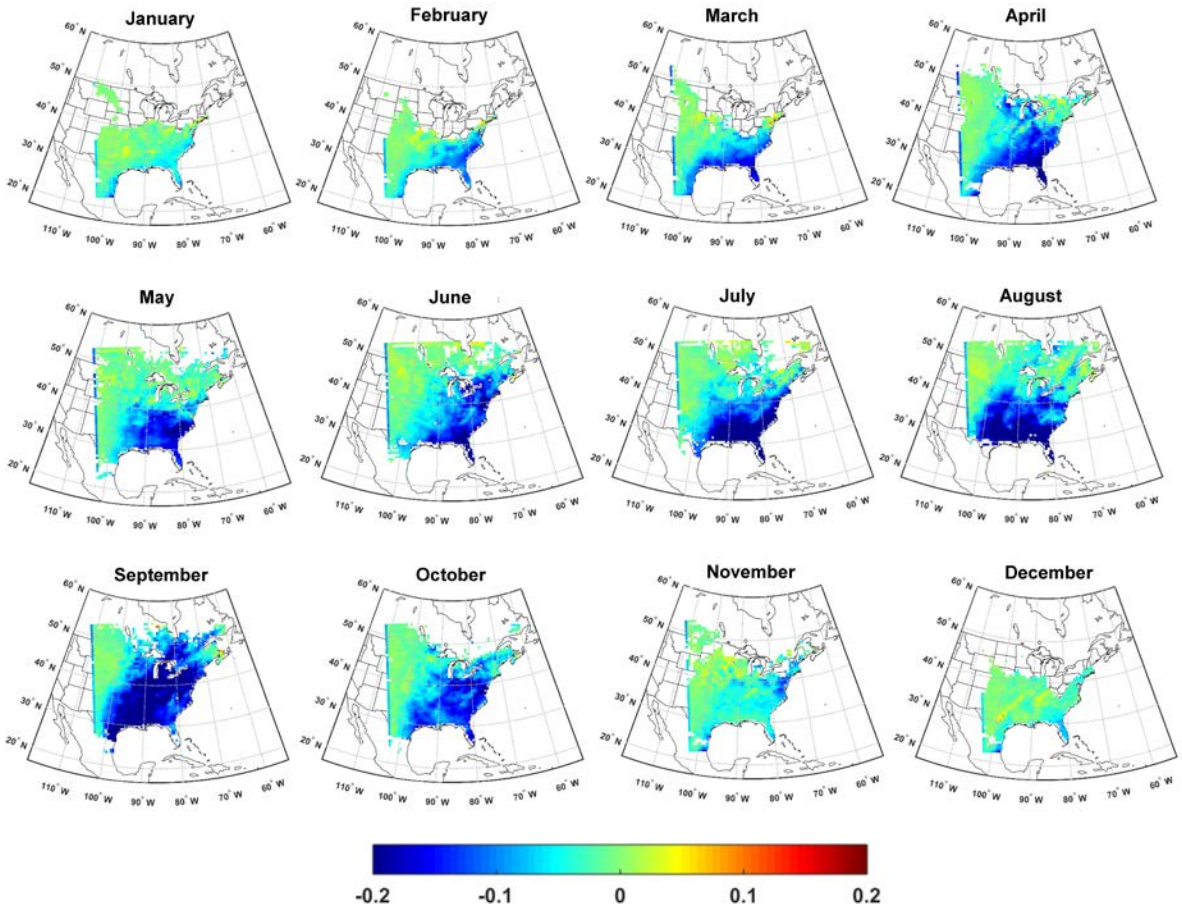

819

820 **Figure 4. Difference in monthly mean AOD at a wavelength (λ) of 550 nm between**
821 **WRF-Chem simulations conducted at 60 km resolution (WRF60) and output from**
822 **WRF-Chem simulations conducted with a resolution of 12 km but remapped to 60 km**
823 **(WRF12-remap). Differences are computed as WRF60 minus WRF12-remap. Similar**
824 **spatial patterns and magnitudes of differences are found for λ of 470 and 660 nm. The**
825 **calendar months of 2008 are shown in the titles of each panel.**

826

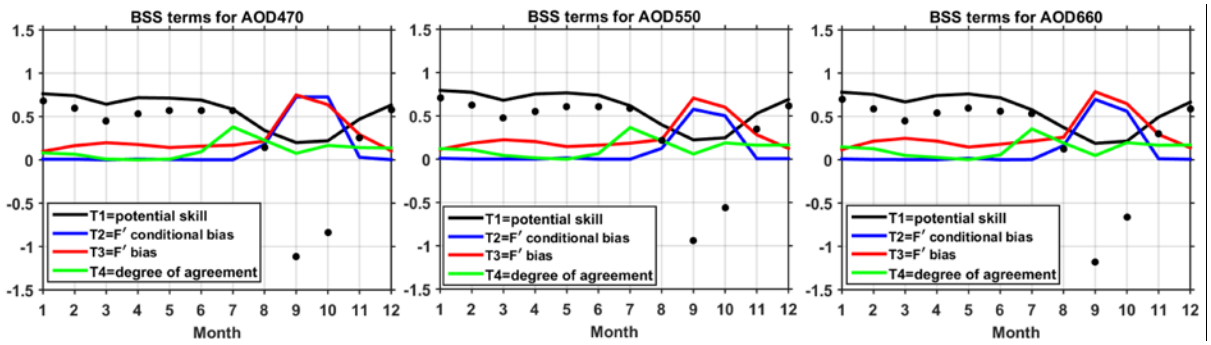

827

828 **Figure 5. Brier Skill Scores (BSS, black dots) for monthly mean AOD by calendar**
829 **month (1=January) for AOD at 470, 550 and 660 nm. In this analysis of model skill**
830 **WRF12 output is mapped to the WRF60 grid (WRF12-remap) and BSS are computed**
831 **using MODIS as the target, WRF60 as the reference forecast and WRF12-remap as the**
832 **forecast. Also shown by the color lines are the contributions of different terms to BSS.**

833

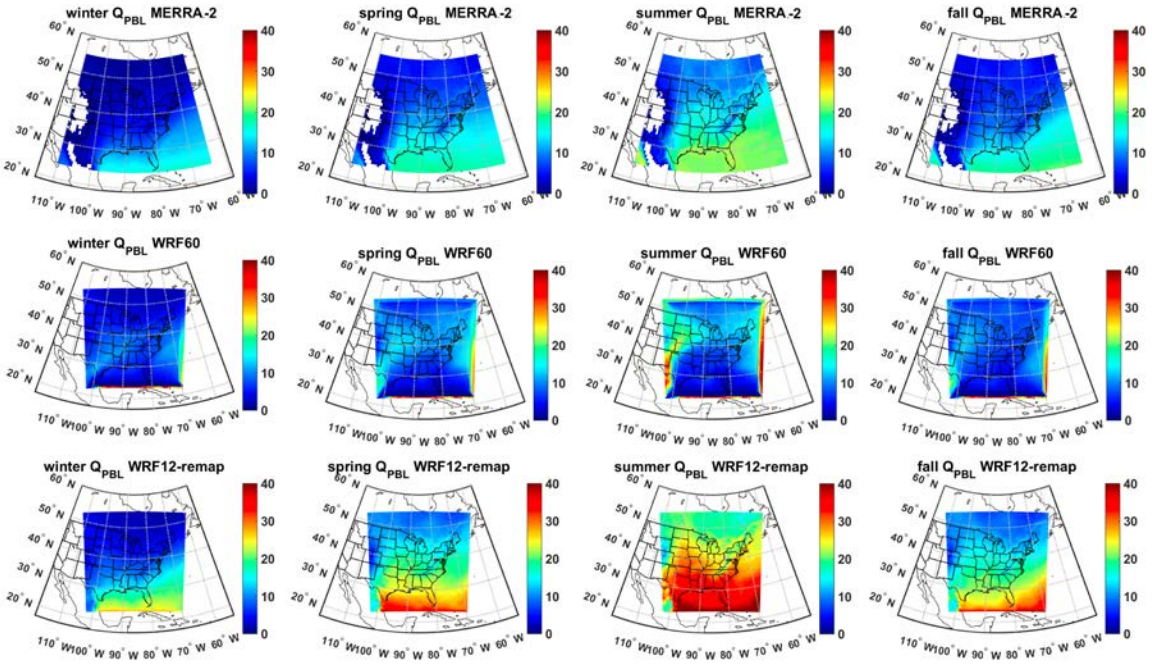

Figure 6. Seasonal mean specific humidity [kg m^{-2}] integrated from the surface to 825 hPa (Q_{PBL}) from MERRA-2 (first row) assuming an average air density in the *PBL* of 1.1 kg m^{-3}, WRF60 (second row), and WRF12-remap (third row). The data are 3-hourly and show only cloud-free hours in all three data sets.

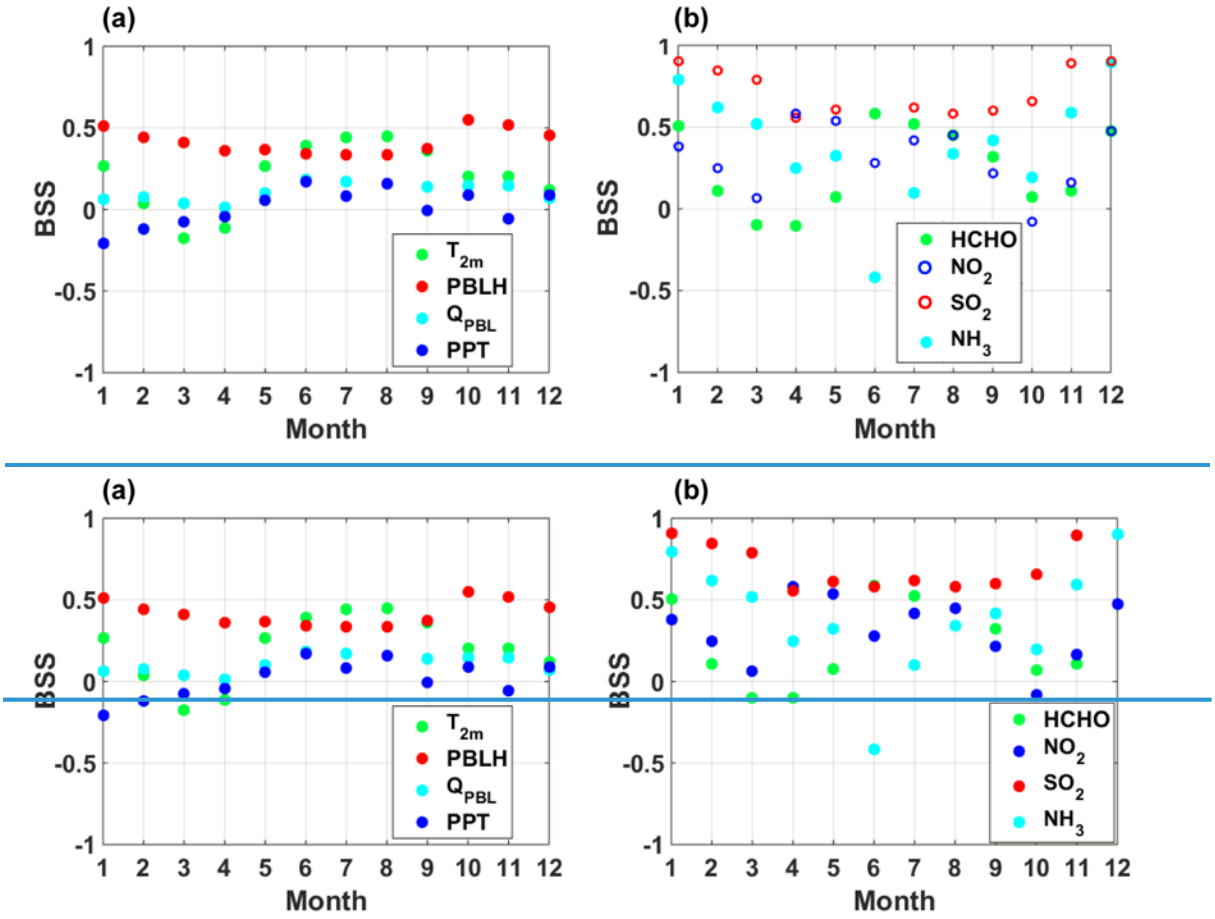

Figure 7. Brier Skill Scores (BSS) for key (a) meteorological and (b) chemical variables. BSS are computed using hourly data of T at 2m (T_{2m}) and *PBLH*, 3-hourly estimates of specific humidity in the boundary layer (Q_{PBL}), and z-scores of monthly total precipitation (*PPT*), and of monthly mean columnar gas phase concentrations.

Tables

Table 1. Physical and chemical schemes adopted in the WRF-Chem simulations presented herein.

Simulation settings	**Values**
Domain size	300 × 300 (60 × 60) grid points
Horizontal resolution	12 km (60 km)
Vertical resolution	32 levels up to 50 hPa
Timestep for physics	72 s (300 s)
Timestep for chemistry	5 s
Physics option	**Adopted scheme**
Microphysics	WRF Single-Moment 5-class (Hong et al., 2004)
Longwave Radiation	Rapid Radiative Transfer Model (RRTM) (Mlawer et al., 1997)
Shortwave Radiation	Goddard (Fast et al., 2006)~~(Chou, 1994){Fast, 2006 #191}~~
Surface layer	Monin Obhukov similarity (Janjić, 2002;Janjić, 1994)
Land Surface	Noah Land Surface Model (Chen and Dudhia, 2001)
Planetary boundary layer	Mellor-Yamada-Janjich (Janjić, 1994)
Cumulus parameterizations	Grell 3 (Grell and Dévényi, 2002)
Chemistry option	**Adopted scheme**
Photolysis	Fast J (Wild et al., 2000)
Gas-phase chemistry	RADM2 (Stockwell et al., 1990)
Aerosols	MADE/SORGAM (Ackermann et al., 1998;Schell et al., 2001)
Anthropogenic emissions	NEI (2005) (US-EPA, 2009)
Biogenic emissions	Guenther, from USGS land use classification (Guenther et al., 1994;Guenther et al., 1993;Simpson et al., 1995)

Table 2. Spearman correlation coefficients (ρ) between AOD at wavelengths (λ) of 470, 550 and 660 nm from MODIS observations averaged over 12 or 60 km and WRF-Chem simulations conducted at 60 km (WRF60, shown in the table as -60), at 12 km (WRF12, shown in the table as -12), and from WRF-Chem simulations at 12 km but remapped to 60 km (WRF12-remap, shown in the table as -remap). Given WRF12-remap is obtained by averaging WRF12 when at least half of the 5×5 12 km resolution cells contain valid data, ρ from WRF60 and WRF12-remap may be computed on slightly different observations and sample size. The bold text denotes correlation coefficients that are significant at α=0.05 after a Bonferroni correction is applied (i.e. $p \le \frac{0.05}{9 \times 12} = 4.63 \times 10^{-4}$ **is significant). The yellow shading is a visual guide that shows for each month and λ the model output that has highest ρ with MODIS.**

Month→/ Variable↓	Jan	Feb	Mar	Apr	May	Jun	Jul	Aug	Sep	Oct	Nov	Dec
470-12	**0.238**	**0.150**	**0.137**	**0.147**	**0.377**	**0.581**	**0.610**	**0.723**	**0.352**	**0.306**	**0.259**	**0.212**
470-60	0.156	**0.226**	**0.438**	**0.412**	**-0.219**	**-0.146**	**0.379**	**0.601**	0.087	-0.051	**0.500**	-0.059
470-remap	**0.295**	**0.197**	**0.250**	**0.182**	**0.516**	**0.637**	**0.675**	**0.777**	**0.368**	**0.441**	**0.315**	**0.274**
550-12	**0.223**	**0.124**	**0.142**	**0.146**	**0.349**	**0.541**	**0.580**	**0.689**	**0.275**	**0.301**	**0.280**	**0.215**
550-60	**0.179**	**0.244**	**0.429**	**0.332**	**-0.288**	**-0.188**	**0.324**	0.567	0.073	-0.077	**0.491**	0.002
550-remap	**0.297**	0.164	**0.261**	**0.199**	**0.493**	**0.605**	**0.651**	**0.747**	**0.286**	**0.437**	**0.352**	**0.309**
660-12	**0.217**	**0.136**	**0.165**	**0.152**	**0.324**	**0.476**	**0.540**	**0.644**	**0.183**	**0.290**	**0.292**	**0.221**
660-60	**0.191**	**0.230**	**0.437**	**0.402**	**-0.305**	**-0.189**	**0.389**	**0.616**	0.099	**-0.137**	**0.536**	0.049
660-remap	**0.356**	**0.211**	**0.289**	**0.208**	**0.480**	**0.624**	**0.669**	**0.772**	**0.371**	**0.432**	**0.393**	**0.368**

Table 3. ~~Table 2.~~ Spatial coherence in the identification of extreme AOD values (i.e. areas with AOD>75th percentile over space for each month) between WRF-Chem at different resolutions relative to MODIS. No significant wavelength dependence is found for model skill in identifying extreme AOD so results are only shown for λ = 550 nm. The different model output is denoted by -60 for simulations at 60 km, -12 for simulations at 12 km resolution, and as –remap for simulations at 12 km but with the output remapped to 60 km. The *Accuracy* (Acc) indicates the fraction of grid cells co-identified as extremes and non-extremes between WRF-Chem and MODIS relative to the total number of cells with valid data. The *Hit Rate* (*HR*) is the probability of correct forecast and is the proportion of cells correctly identified as extremes by both WRF-Chem and MODIS. The yellow shading indicates the model resolution with highest skill in each month for AOD at 550 nm.

Month→/ Metric↓	Jan	Feb	Mar	Apr	May	Jun	Jul	Aug	Sep	Oct	Nov	Dec
Acc-12	0.673	0.665	0.659	0.638	0.710	0.800	0.855	0.839	0.666	0.679	0.723	0.661
Acc-60	0.707	0.778	0.735	0.730	0.600	0.587	0.658	0.769	0.661	0.637	0.729	0.681
Acc-remap	0.674	0.680	0.694	0.640	0.766	0.824	0.887	0.837	0.667	0.699	0.767	0.641
HR-12	0.346	0.331	0.319	0.275	0.421	0.599	0.711	0.678	0.333	0.358	0.447	0.323
HR-60	0.417	0.558	0.471	0.460	0.200	0.173	0.315	0.538	0.321	0.274	0.458	0.364
HR-remap	0.350	0.361	0.387	0.281	0.532	0.649	0.775	0.674	0.333	0.399	0.535	0.284

Supplementary Materials for the manuscript:

Value-added by high-resolution regional simulations of climate-relevant aerosol properties

P. Crippa[1], R. C. Sullivan[2], A. Thota[3], S. C. Pryor[2,3]

[1] COMET, School of Civil Engineering and Geosciences, Cassie Building, Newcastle University, Newcastle upon Tyne, NE1 7RU, UK

[2] Department of Earth and Atmospheric Sciences, Bradfield Hall, 306 Tower Road, Cornell University, Ithaca, NY 14853, USA

[3] Pervasive Technology Institute, Indiana University, Bloomington, IN 47405, USA

Table S1. Physical and chemical schemes adopted in the WRF-Chem simulations presented herein.

Simulation settings	**Values**
Domain size	300 × 300 (60 × 60) grid points
Horizontal resolution	12 km (60 km)
Vertical resolution	32 levels up to 50 hPa
Timestep for physics	72 s (300 s)
Timestep for chemistry	5 s
Physics option	**Adopted scheme**
Microphysics	WRF Single-Moment 5-class
Longwave Radiation	Rapid Radiative Transfer Model (RRTM)
Shortwave Radiation	Goddard
Surface layer	Monin-Obhukov similarity
Land Surface	Noah Land Surface Model
Planetary boundary layer	Mellor-Yamada-Janjich
Cumulus parameterizations	Grell 3
Chemistry option	**Adopted scheme**
Photolysis	Fast J
Gas-phase chemistry	RADM2
Aerosols	MADE/SORGAM
Anthropogenic emissions	NEI (2005)
Biogenic emissions	Guenther, from USGS land use classification

Table S12. Ratio of spatial variability (i.e. the standard deviation of AOD computed across all grid cells) between AOD at wavelengths (λ) of 470, 550 and 660 nm from MODIS observations mapped at 60 km and WRF-Chem simulations conducted at 60 km resolution (WRF60, shown in the table as -60), at 12 km resolution (WRF12, shown in the table as -12), and from WRF-Chem simulations at 12 km but remapped to 60 km (WRF12-remap, shown in the table as -remap). Given WRF12-remap is obtained by averaging WRF12 when at least half of the 5×5 12 km resolution cells contain valid data, the ratio of standard deviations from WRF60 and WRF12-remap may be computed on slightly different observations and sample size. The yellow shading shows for each month and λ the model with ratio of standard deviations closer to 1.

Month→/ Variable↓	Jan	Feb	Mar	Apr	May	Jun	Jul	Aug	Sep	Oct	Nov	Dec
470-12	0.489	0.581	0.382	0.595	0.806	0.802	1.033	1.20	1.935	1.698	0.766	0.457
470-60	0.615	0.717	0.682	0.648	0.556	0.331	0.353	0.291	0.541	0.605	0.562	0.564
470-remap	0.522	0.630	0.380	0.644	0.993	0.791	1.018	1.194	2.079	2.099	0.853	0.512
550-12	0.406	0.475	0.307	0.480	0.630	0.690	0.996	1.106	1.709	1.401	0.663	0.370
550-60	0.578	0.663	0.629	0.624	0.502	0.302	0.327	0.274	0.480	0.525	0.518	0.505
550-remap	0.431	0.503	0.299	0.524	0.764	0.693	0.990	1.110	1.872	1.758	0.745	0.396
660-12	0.401	0.454	0.283	0.462	0.571	0.671	1.004	1.114	1.684	1.343	0.665	0.351
660-60	0.458	0.531	0.497	0.462	0.378	0.214	0.225	0.184	0.328	0.391	0.402	0.405
660-remap	0.342	0.393	0.235	0.391	0.553	0.474	0.676	0.777	1.369	1.331	0.557	0.307

Table ~~S3~~S2. Spatial coherence in the identification of hourly precipitation between WRF-Chem at different resolutions relative to MERRA-2. The Hit Rate (*HR*) indicates the probability of correct forecast and is the proportion of cells correctly identified as with precipitation by both WRF-Chem and MERRA-2. The Mean Fractional Bias (MFB) in space is also reported for each month and computed from the hourly precipitation rates. The yellow shading indicates the model resolution with highest HR and lower absolute MFB in each month for precipitation.

Month→/ Metric↓	Jan	Feb	Mar	Apr	May	Jun	Jul	Aug	Sep	Oct	Nov	Dec
HR-60	0.344	0.298	0.228	0.122	0.083	0.072	0.057	0.059	0.067	0.078	0.154	0.218
HR-remap	0.698	0.715	0.680	0.539	0.402	0.440	0.479	0.438	0.438	0.454	0.581	0.666
MFB-60	-0.340	-0.347	-0.384	-0.442	-0.462	-0.468	-0.475	-0.474	-0.469	-0.459	-0.423	-0.385
MFB-12	-0.095	-0.068	-0.065	-0.168	-0.273	-0.269	-0.260	-0.274	-0.281	-0.261	-0.170	-0.119

Figure S1. Seasonal mean of hourly temperature at 2 meters [K] from MERRA-2 (first row), WRF60 (second row), and WRF12-remap (third row), for simultaneous data from all three datasets.

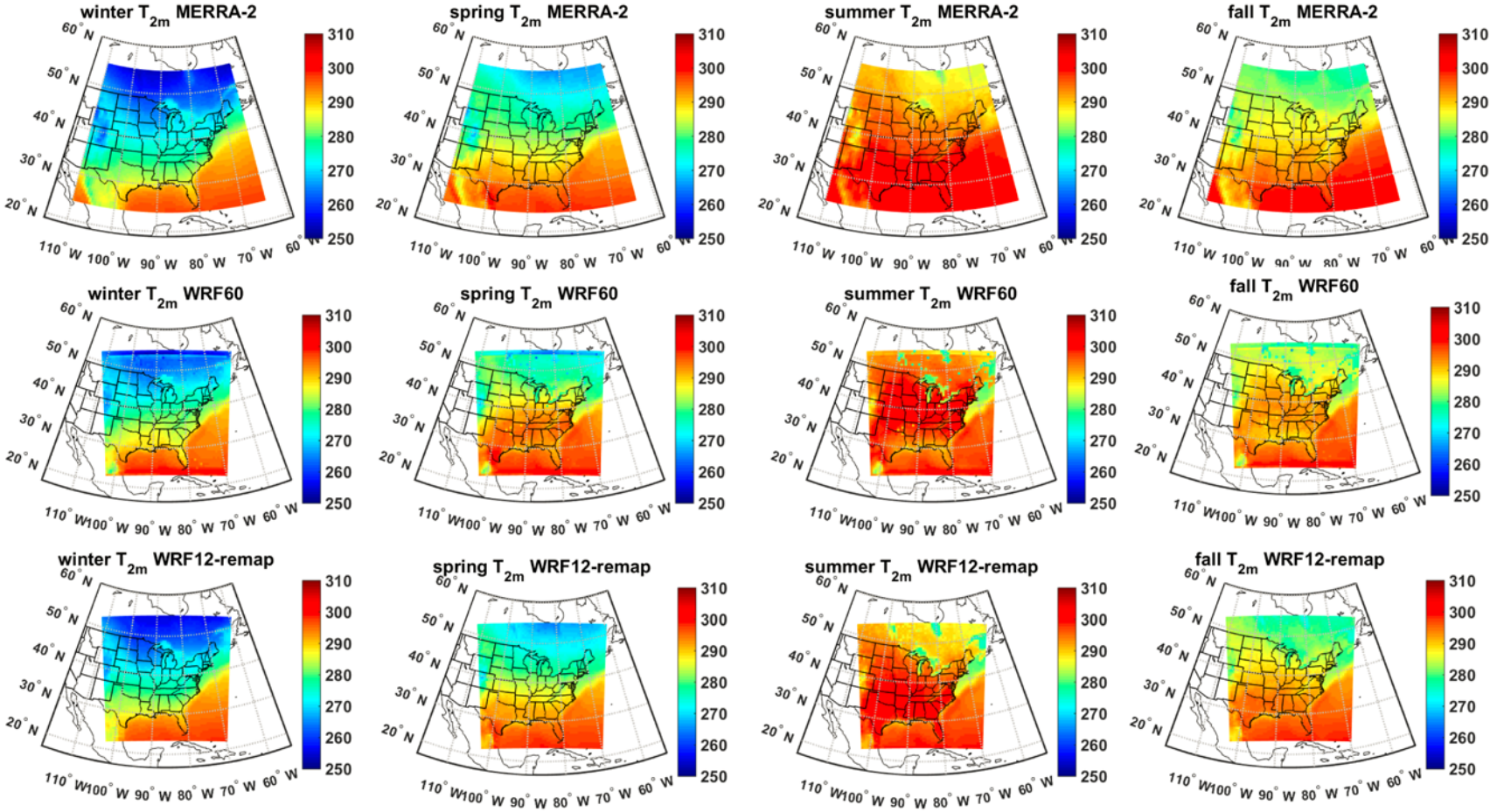

Figure S2. Seasonal average of hourly Planetary Boundary Layer Height, *PBLH* [m] from MERRA-2 (first row), WRF60 (second row), and WRF12-remap (third row), for simultaneous hours of the three datasets.

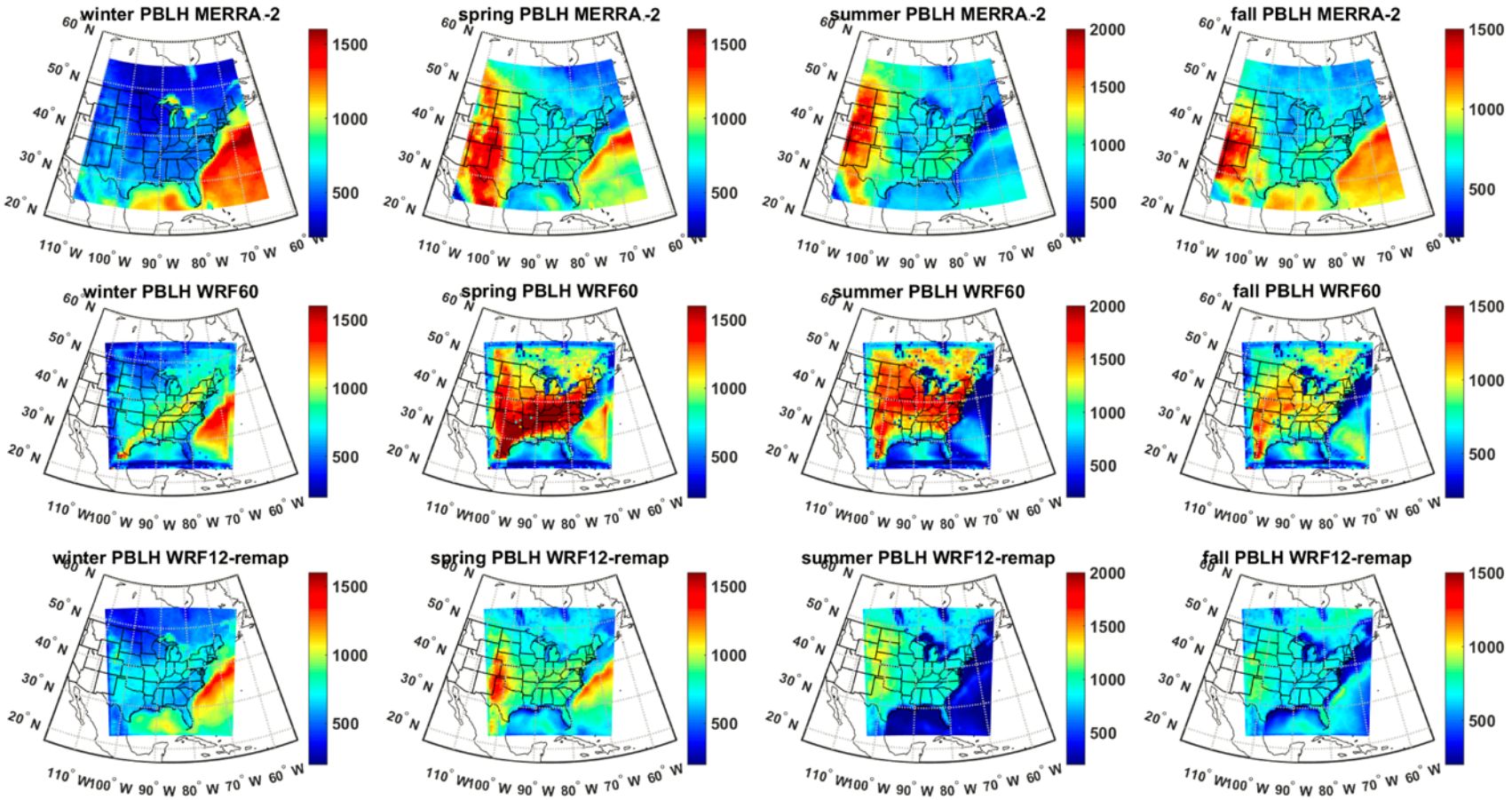

Figure S3. Seasonal total precipitation (mm) from MERRA-2 (first row), WRF60 (second row), and WRF12-remap (third row).

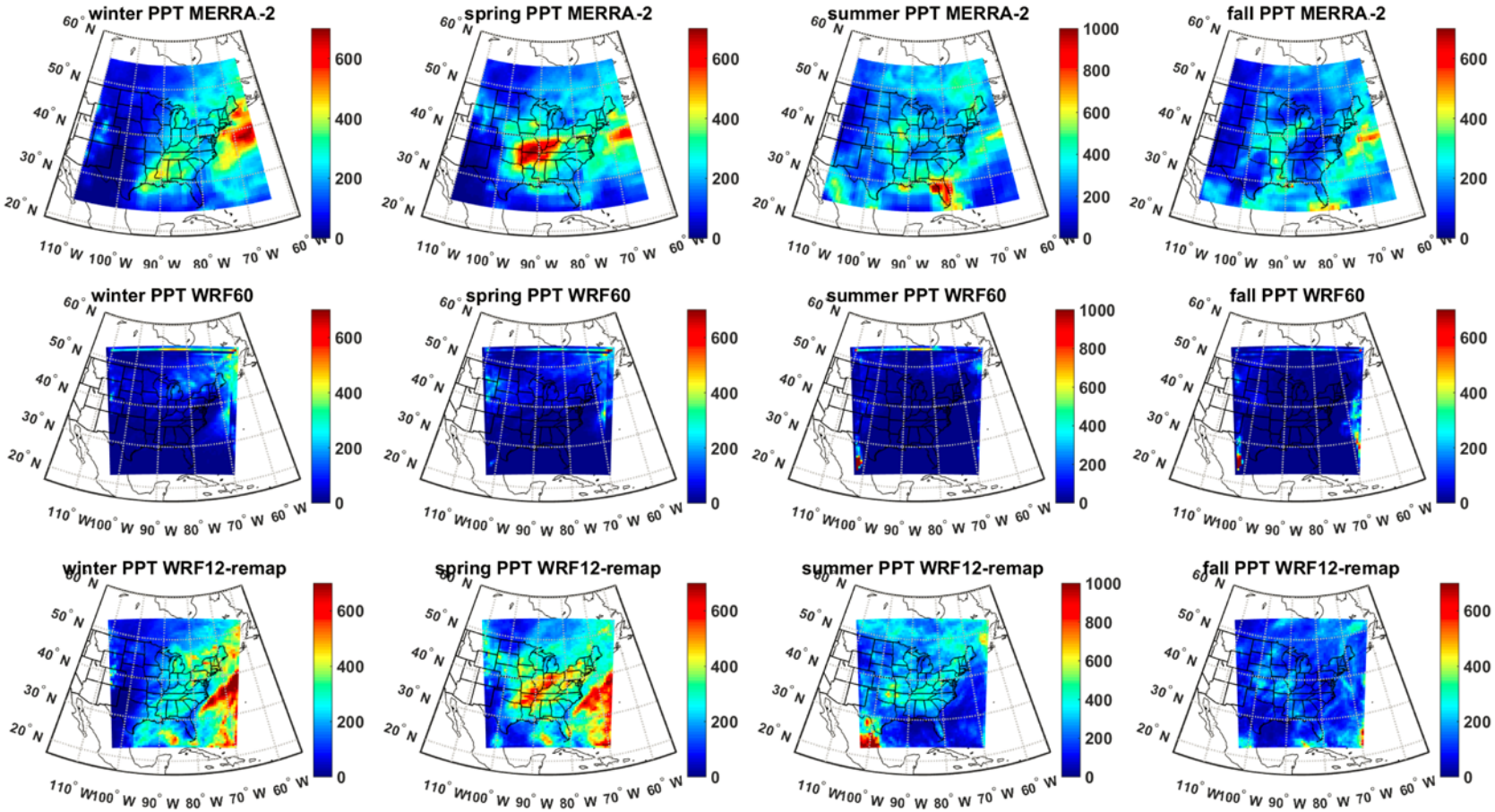

Figure S4. Seasonal total column SO_2 z-scores from OMI (first row), WRF60 (second row), and WRF12-remap (third row). z-scores are computed relative to the spatial seasonal mean of each dataset and indicate the distance from the mean in terms of standard deviation units. A cloud screen of 0.3 is applied to both satellite observations and simulated values. Only grid cells with at least 5 valid observations in a month are used to compute a mean value, otherwise the grid cell is shown as white.

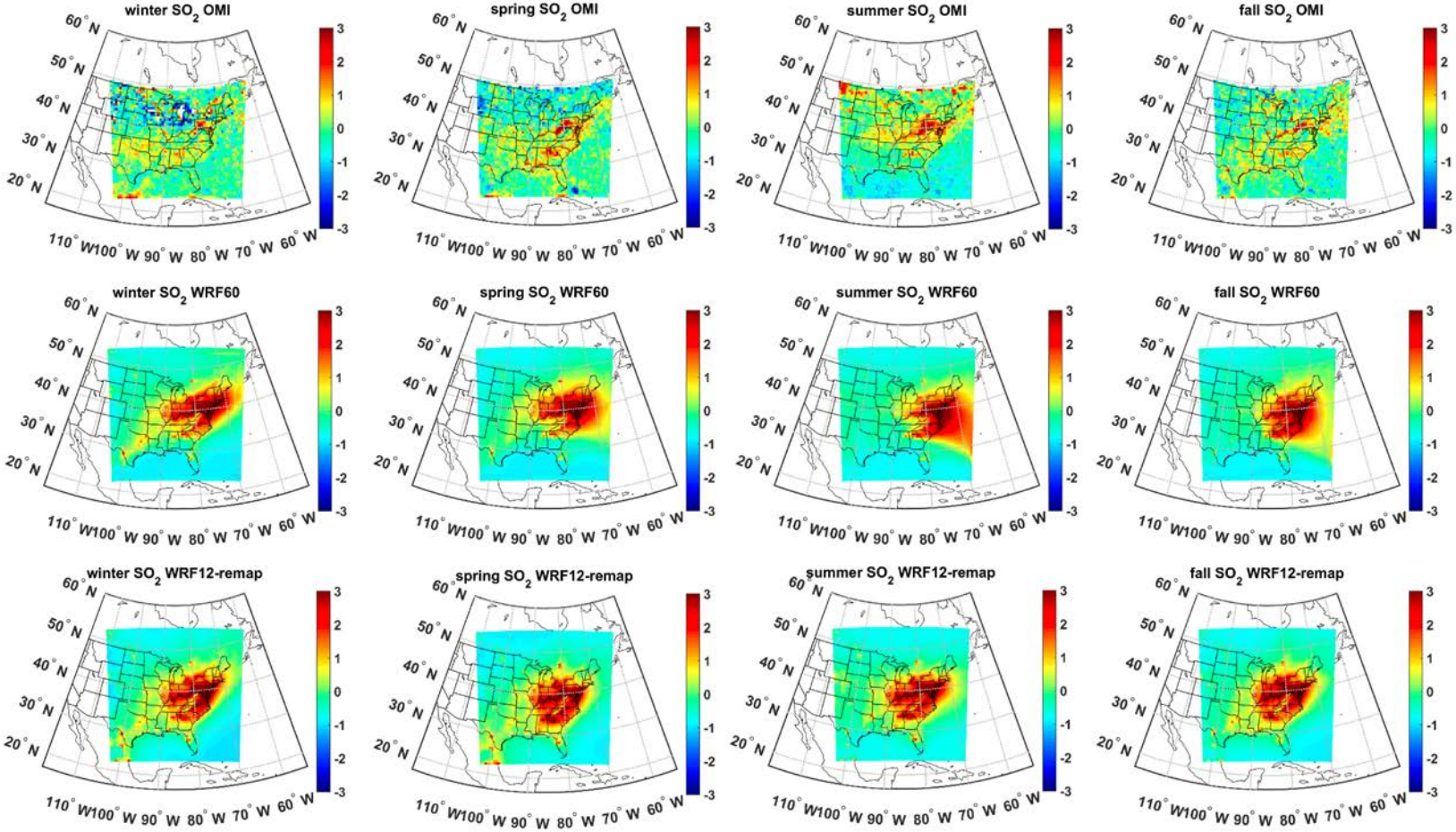

Figure S5. Seasonal total column NO_2 z-scores from OMI (first row), WRF60 (second row), and WRF12-remap (third row). z-scores are computed relative to the spatial seasonal mean of each dataset and indicate the distance from the mean in terms of standard deviation units. A cloud screen of 0.3 is applied to both satellite observations and simulated values. Only grid cells with at least 5 valid observations in a month are used to compute a mean value, otherwise the grid cell is shown as white.

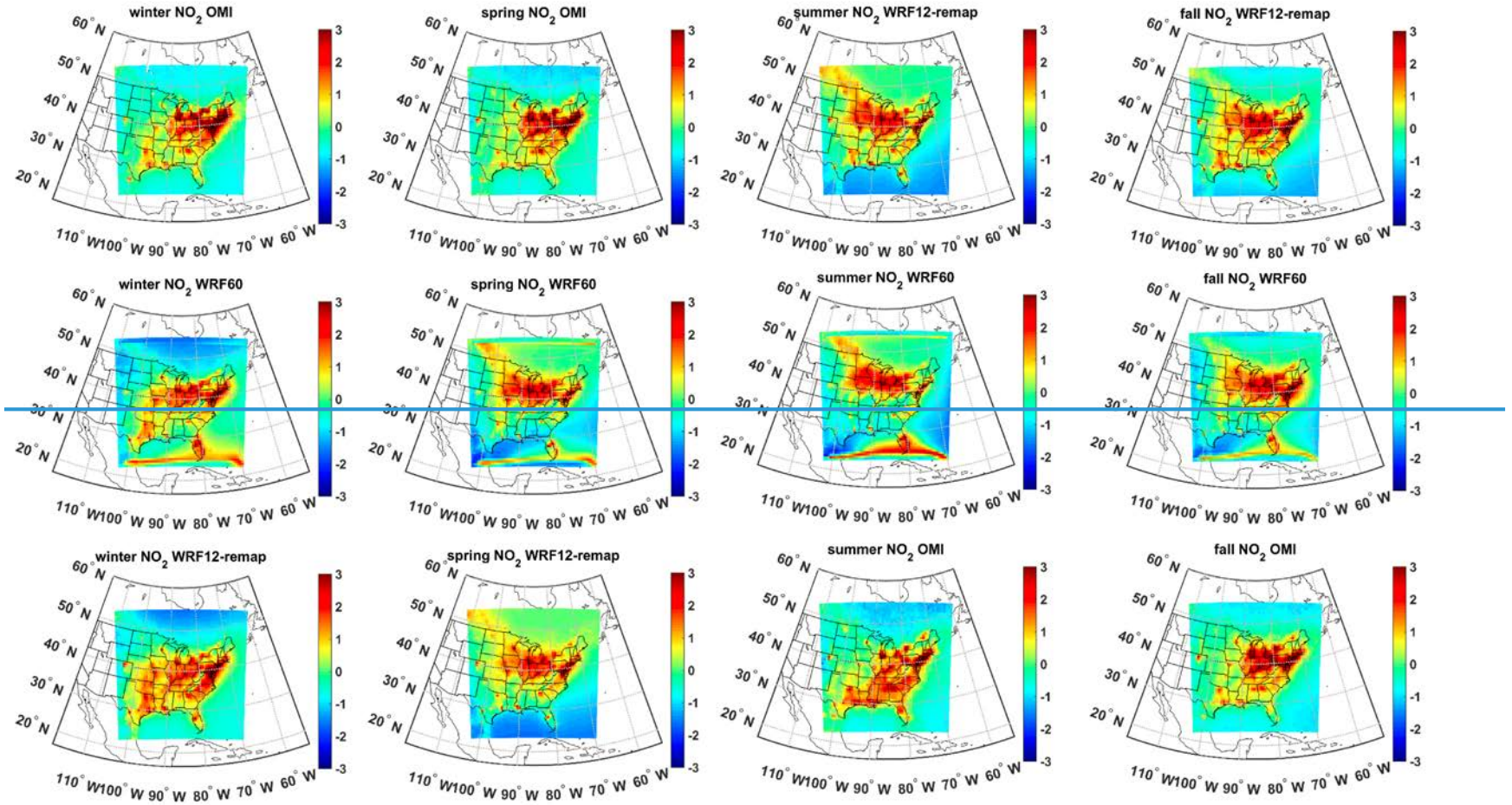
winter NO2 OMI
spring NO2 OMI
summer NO2 WRF12-remap
fall NO2 WRF12-remap
winter NO2 WRF60
spring NO2 WRF60
summer NO2 WRF60
fall NO2 WRF60
winter NO2 WRF12-remap
spring NO2 WRF12-remap
summer NO2 OMI
fall NO2 OMI
60°N
50°N
40°N
30°N
20°N
110°W 100°W 90°W 80°W 70°W 60°W
3
2
1
0
-1
-2
-3

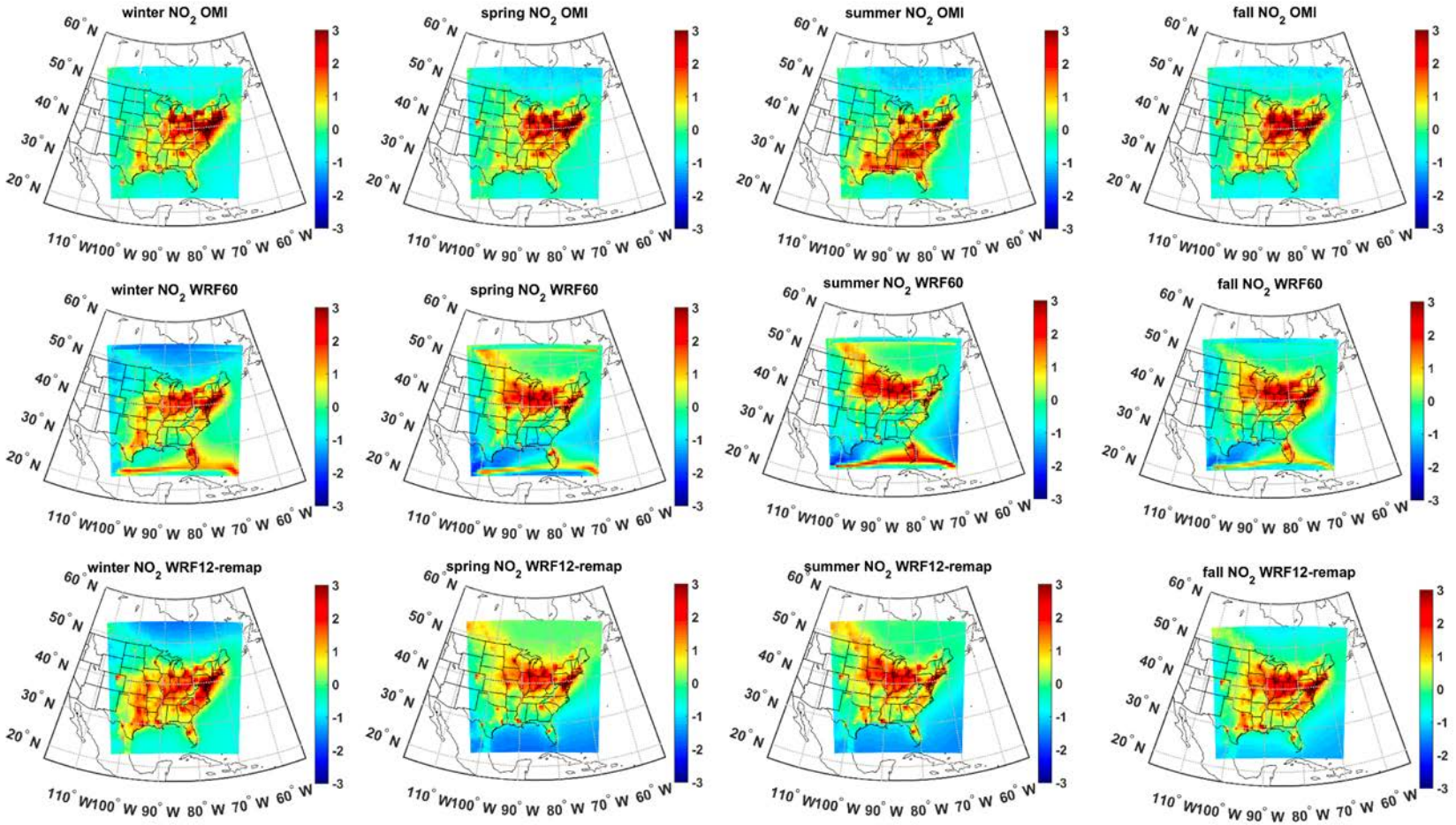

Figure S6. Seasonal total column NH_3 z-scores from OMI (first row), WRF60 (second row), and WRF12-remap (third row). z-scores are computed relative to the spatial seasonal mean of each dataset and indicate the distance from the mean in terms of standard deviation units. A cloud screen of 0.3 is applied to both satellite observations and simulated values. Only grid cells with at least 5 valid observations in a month are used to compute a mean value, otherwise the grid cell is shown as white.

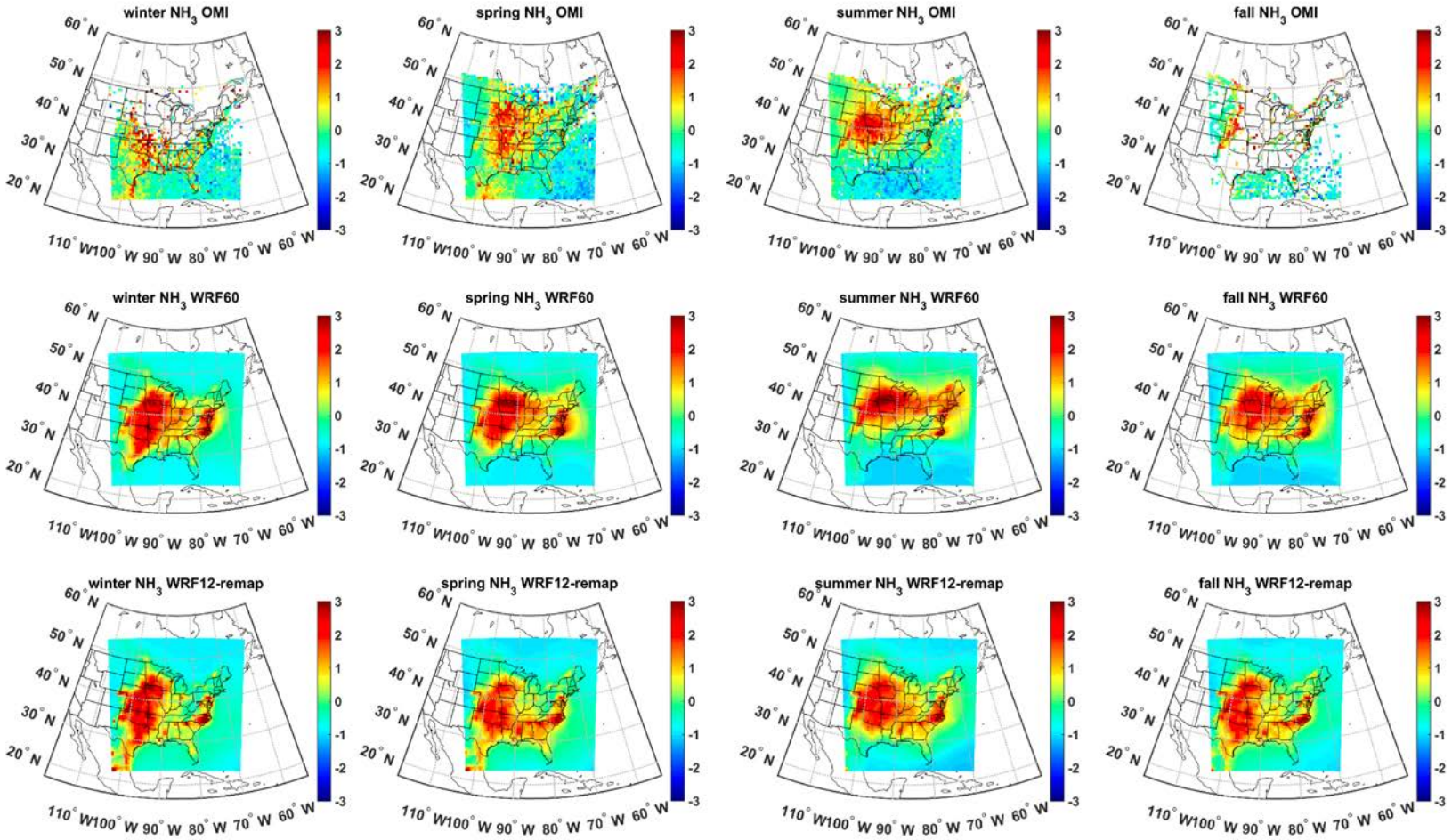

Figure S7. Seasonal total column HCHO z-scores from OMI (first row), WRF60 (second row), and WRF12-remap (third row). z-scores are computed relative to the spatial seasonal mean of each dataset and indicate the distance from the mean in terms of standard deviation units. A cloud screen of 0.3 is applied to both satellite observations and simulated values. Only grid cells with at least 5 valid observations in a month are used to compute a mean value, otherwise the grid cell is shown as white.

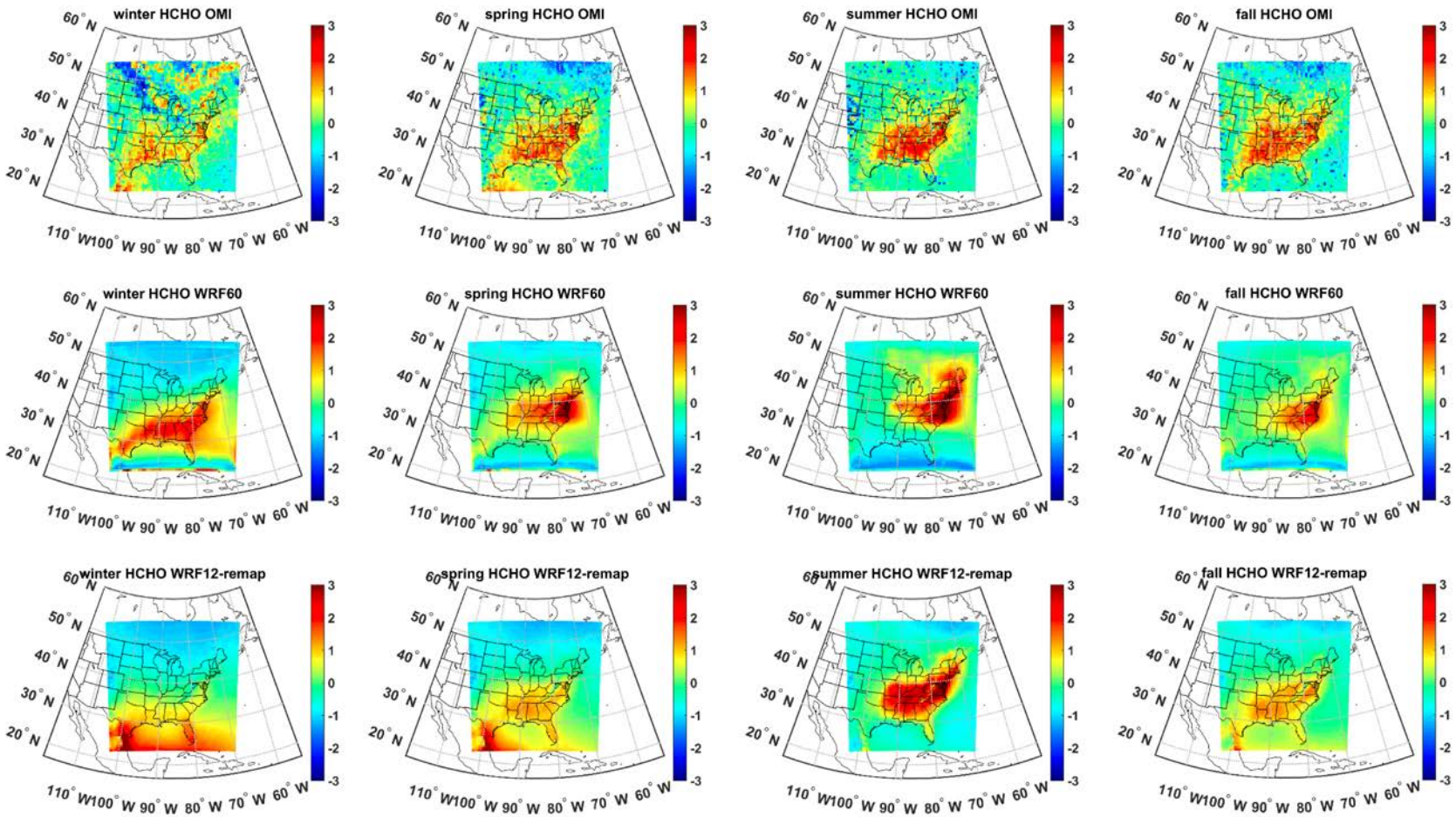
winter HCHO OMI
spring HCHO OMI
summer HCHO OMI
fall HCHO OMI
winter HCHO WRF60
spring HCHO WRF60
summer HCHO WRF60
fall HCHO WRF60
winter HCHO WRF12-remap
spring HCHO WRF12-remap
summer HCHO WRF12-remap
fall HCHO WRF12-remap
60° N
50° N
40° N
30° N
20° N
110° W
100° W
90° W
80° W
70° W
60° W
3
2
1
0
-1
-2
-3